

Magneto-optical Kerr effect in Weyl semimetals with broken inversion and time-reversal symmetries

Olivier Trépanier,¹ Rémi N. Duchesne,¹ Jérémie J. Boudreault,¹ and René Côté¹

¹*Département de physique and Institut Quantique,
Université de Sherbrooke, Sherbrooke, Québec, Canada J1K 2R1
(Dated: August 30, 2022)*

The topological nature of the band structure of a Weyl semimetal leads to a number of unique transport and optical properties. For example, the description of the propagation of an electromagnetic wave in a Weyl semimetal with broken time-reversal and inversion symmetry, for example, requires a modification of the Maxwell equations by the axion field $\theta(\mathbf{r}, t) = 2\mathbf{b} \cdot \mathbf{r} - 2b_0t$, where $2\mathbf{b}$ is the separation in wave vector space between two Weyl nodes of opposite chiralities and $2\hbar b_0$ is their separation in energy. In this paper, we study theoretically how the axion terms b_0 and \mathbf{b} modify the frequency behavior of the Kerr rotation and ellipticity angles $\theta_K(\omega)$ and $\psi_K(\omega)$ in a Weyl semimetal. Both the Faraday and Voigt configurations are considered since they provide different information on the electronic transitions and plasmon excitation. We derive the Kerr angles firstly without an external magnetic field where the rotation of the polarization is only due to the axion terms and secondly in a strong magnetic field where these terms compete with the gyration effect of the magnetic field. In this latter case, we concentrate on the ultra-quantum limit where the Fermi level lies in the chiral Landau level and the Kerr and ellipticity angles have more complex frequency and magnetic field behaviors.

I. INTRODUCTION

A Weyl semimetal¹ (WSM) is a three-dimensional topological phase of matter where pairs of nondegenerate bands cross at isolated points in the Brillouin zone called "Weyl nodes". Near these points, the electronic dispersion is gapless and linear in wave vector. The electrons in each node are described by the Weyl equation which is a two-component analog of the Dirac equation and to each node is associated a chirality index $\chi = \pm 1$ which reflects the topological nature of the band structure. The Nielsen-Ninomiya theorem² requires that the number of Weyl points in the Brillouin zone be even so that Weyl nodes must occur in pairs of opposite chiralities. Stability of the Weyl nodes requires that time-reversal and/or inversion symmetry be broken. If both symmetries are broken, the minimal number of Weyl nodes is two.

The topological nature of the band structure of a WSM leads to a number of interesting transport and optical properties such as an anomalous Hall effect³, the chiral-magnetic effect⁴, Fermi arcs⁵, a chiral anomaly leading to a negative longitudinal negative magnetoresistance⁶ and to a plasmon⁷ whose frequency increases with the magnetic field B as \sqrt{B} .

Valuable information on the band structure and topological properties of WSMs can be obtained by magneto-optical methods such as the magneto-optical Kerr effect (MOKE)⁸ which is a powerful probe of the magnetic and electronic properties of a material. The MOKE is a non-contact technique that measures the rotation of the polarization vector and the ellipticity of an electromagnetic wave reflected from the surface of a material. The rotation is due to the presence of off-diagonal elements in the dielectric tensor of a material that are caused by an external magnetic field and, in WSMs, by the axion terms b_0 and \mathbf{b} in addition to the magnetic field. The transmission

analog of the MOKE, the Faraday effect, has been shown to be very large in some WSMs⁹ and, as we demonstrate in this paper, it is also the case for the Kerr effect.

In order to study the optical properties of WSMs, one must take into account the fact that the source terms in Maxwell equations are modified by the axion field $\theta(\mathbf{r}, t) = 2\mathbf{b} \cdot \mathbf{r} - 2b_0t$, where $2\hbar\mathbf{b}$ is the separation in momentum space between two Weyl nodes of opposite chiralities and $2\hbar b_0$ is their separation in energy¹⁰⁻¹². The axion terms generate an extra current $\mathbf{j} = -\frac{e^2}{2\pi^2\hbar}\mathbf{b} \times \mathbf{E} + \frac{e^2}{2\pi^2\hbar}b_0\mathbf{B}$ in the Ampère-Maxwell equation and an extra density $\rho = \frac{2\alpha}{\pi}\sqrt{\frac{\varepsilon_0}{\mu_0}}\mathbf{b} \cdot \mathbf{B}$ in the Gauss law (here, $\alpha = e^2/4\pi\varepsilon_0\hbar c$ is the fine-structure constant and ε_0, μ_0 are the permittivity and permeability of free space). The first axion term, \mathbf{b} , is present if time-reversal symmetry is broken and is responsible for the anomalous Hall effect while the second axion term, b_0 , breaks space-inversion symmetry and leads to the chiral magnetic effect. Even in the absence of a magnetic field, a WSM has a gyrotropic property if \mathbf{b} or (to a lesser extent) b_0 is non-zero (as we will show, the rotating power of b_0 is negligible in comparison with that of \mathbf{b}).

The effect of the axion term \mathbf{b} on the Kerr and Faraday rotations has been studied previously¹³ using a simple, undoped, two-node model of a WSM with broken time-reversal symmetry and in zero magnetic field. This work has subsequently been extended to include doping and tilting of the Weyl cones in Ref. 14 where the authors predicted a giant Kerr angle of the order of 0.1 rad for optical frequencies below 10 THz in both type-I and type-II thin films of Weyl semimetals. They also found a large Kerr effect caused by the axion term \mathbf{b} in a bulk WSM. In a previous paper by one of us¹⁵, it was shown that the MOKE in a Weyl semimetal with time-reversal symmetry (i.e., $\mathbf{b} = 0$) and tilted Weyl cones in a strong magnetic

field is modified in comparison with its behavior in a normal metal. It was also shown that a valley polarization¹⁶ can be detected in the MOKE signal which also bears a signature of the chiral anomaly in the form of a large peak at the plasmon frequency in the Kerr angle in the Voigt configuration. This peak is blueshifted as $\omega \sim \sqrt{B}$ as expected⁷.

In this paper, we study the frequency and magnetic field behaviors of the Kerr and ellipticity angles $\theta_K(\omega, B)$ and $\psi_K(\omega, B)$ in a WSM with broken time-reversal and inversion symmetries with: 1) the axion terms \mathbf{b} and b_0 alone (i.e., the natural gyrotropy of the WSM) and 2) in the presence of a strong magnetic field where these terms compete with the gyrotropy that the magnetic field induces. We work at $T = 0$ K with a two-node model, the simplest possible in order to get the essential physics. We allow for doping so that, in conjunction with b_0 , the WSM can be electron or hole doped or at compensation. The Dirac cones are untilted and the WSM is in equilibrium with a common Fermi level e_F for both nodes.

In a strong magnetic field, the electronic energy is quantized into a set of negative and positive energy levels $n = 0, \pm 1, \pm 2, \dots$. An important characteristic of a WSM is the presence of a single linearly dispersive chiral Landau level (the $n = 0$ level) at each node where the electrons disperse in only one direction which is dictated by the chirality index χ of the node. This chiral Landau level modifies the dielectric tensor and so the optical properties of a WSM. This is especially true in the ultra-quantum regime where the Fermi level e_F lies in this chiral level. The lowest-energy electronic transitions are then given by the frequencies $\omega_{n,m}$ with $n = -1, m = 0$ and $n = 0, m = 1$. In this regime, the Kerr angle is particularly interesting. Indeed, we find a plateau where $\theta_K(\omega) = \pi/2$ and another one where $\theta_K(\omega) = 0$ when ω is smaller than the value $\min(\omega_{-1,0}, \omega_{0,1})$ i.e., in the Pauli blocked regime. We also find that for the special case where $b\hbar v_F = e_F$ for $\mathbf{b} \parallel \mathbf{B}$ and $b_0 = 0$ (v_F is the Dirac-Weyl velocity), the Kerr angle is exactly zero for $\omega \in [0, \min(\omega_{-1,0}, \omega_{0,1})]$.

In a magnetic field, two configurations are usually studied¹⁷. One is the Faraday configuration where the incident light propagates along the direction of the magnetic field \mathbf{B} with its polarization vector perpendicular to \mathbf{B} and the Voigt configuration where the propagation is perpendicular to \mathbf{B} but the polarization vector has a component along \mathbf{B} . The two configurations give different information on the system capturing, for example, different electronic transitions. In a WSM, we find that the plasmon mode has a signature in $\theta_K(\omega)$ in the Voigt configuration only if $\mathbf{b} \parallel \mathbf{B}$ while it is signaled in both configurations if \mathbf{b} is tilted with respect to \mathbf{B} .

The remainder of this paper is organized as follows: we derive the dielectric tensor of a WSM with and without magnetic field in Sections II and III. Section IV discusses the modification of the Maxwell equations by the axion terms. We introduce the formalism necessary to compute the Kerr and ellipticity angles in the Faraday and Voigt

configurations in Sec. V. We briefly review the Kerr rotation for a normal metal in Sec. VI and then present our numerical results for the frequency dependence of the Kerr angle in a WSM with and without magnetic field in Secs. VII and VIII. We study the effect of tilting the vector \mathbf{b} with respect to the magnetic field in Sec. IX. In Section X, we discuss the magnetic field and \mathbf{b} dependence (for $\mathbf{b} \parallel \mathbf{B}$) of the Kerr angle in the Faraday configuration. We conclude in Sec. XI.

II. DIELECTRIC TENSOR OF A WSM IN ZERO MAGNETIC FIELD

We consider a simple two-node model of a Weyl semimetal (WSM) with broken space-inversion and time-reversal symmetries so that the two nodes have opposite chiralities. The nodes are centered at wave vectors $-\chi\mathbf{b}$, where $\chi = \pm 1$ is the chirality index. The Hamiltonian of the electron gas in each Weyl node is given by

$$h_\chi(\mathbf{k}) = \chi\hbar v_F \mathbf{k} \cdot \boldsymbol{\sigma} + \chi\hbar b_0 I_2, \quad (1)$$

where v_F is the Dirac-Weyl velocity, \mathbf{k} is the wave vector measured from the position of the Weyl node, $\boldsymbol{\sigma}$ is the vector of Pauli matrices defined in the basis of the two electronic bands that cross, I_2 is the 2×2 unit matrix, $2\hbar b_0$ is the separation in energy of the two Dirac points, and $2\hbar\mathbf{b}$ is their separation in momentum space. The former term breaks the space-inversion symmetry while the latter breaks time-reversal symmetry.

The energy spectrum is given by

$$E_{\chi,s}(\mathbf{k}) = s\hbar v_F |\mathbf{k}| + \chi\hbar b_0, \quad (2)$$

where $s = \pm 1$ is the band index i.e., the upper ($s = +$) or lower part ($s = -$) of the Dirac cone. The corresponding eigenvectors are of the form $v_{\chi,\mathbf{k},s}(\mathbf{r}) = \frac{1}{\sqrt{V}} \eta_{\chi,s}(\mathbf{k}) e^{i\mathbf{k} \cdot \mathbf{r}}$, where V is the volume of the WSM and the spinors $\eta_{\chi,s}(\mathbf{k})$ are given by

$$\eta_{+,-}(\mathbf{k}) = \eta_{-,-}(\mathbf{k}) = \begin{pmatrix} e^{-i\varphi_{\mathbf{k}}/2} \cos\left(\frac{\theta_{\mathbf{k}}}{2}\right) \\ e^{i\varphi_{\mathbf{k}}/2} \sin\left(\frac{\theta_{\mathbf{k}}}{2}\right) \end{pmatrix}, \quad (3)$$

$$\eta_{+,-}(\mathbf{k}) = \eta_{-,+}(\mathbf{k}) = \begin{pmatrix} -e^{-i\varphi_{\mathbf{k}}/2} \sin\left(\frac{\theta_{\mathbf{k}}}{2}\right) \\ e^{i\varphi_{\mathbf{k}}/2} \cos\left(\frac{\theta_{\mathbf{k}}}{2}\right) \end{pmatrix}, \quad (4)$$

where $\theta_{\mathbf{k}}, \varphi_{\mathbf{k}}$ are respectively the polar and azimuthal angles of the wave vector \mathbf{k} .

To derive the many-body Hamiltonian, we define the field operators

$$\Psi_\chi(\mathbf{r}) = \frac{1}{\sqrt{V}} \sum_{s,\mathbf{k}} e^{i\mathbf{k} \cdot \mathbf{r}} \eta_{\chi,s}(\mathbf{k}) c_{\chi,s,\mathbf{k}}. \quad (5)$$

The operators $c_{\chi,s,\mathbf{k}}, c_{\chi,s,\mathbf{k}}^\dagger$ annihilate or create an electron in state (χ, s, \mathbf{k}) . They satisfy the commutation re-

lation $\{c_{\chi,s,\mathbf{k}}, c_{\chi',s',\mathbf{k}'}^\dagger\} = \delta_{\chi,\chi'}\delta_{s,s'}\delta_{\mathbf{k},\mathbf{k}'}$. The second-quantized Hamiltonian for each node is then

$$\begin{aligned} H_\chi &= \int d^3r \Psi_\chi^\dagger(\mathbf{r}) h_\chi(\mathbf{k}) \Psi_\chi(\mathbf{r}) \\ &= \sum_{s,\mathbf{k}} E_{\chi,s}(\mathbf{k}) c_{\chi,s,\mathbf{k}}^\dagger c_{\chi,s,\mathbf{k}}. \end{aligned} \quad (6)$$

The current operator is obtained, after making the Peierls substitution $h_\chi(\mathbf{k}) \rightarrow h_\chi(\mathbf{k} + e\mathbf{A}/\hbar)$ in the hamiltonian ($e > 0$ for an electron and \mathbf{A}_e is the vector potential of an external electromagnetic field), by taking the derivative

$$\mathbf{j}_\chi = -\frac{\delta h_\chi}{\delta \mathbf{A}_e} = -\chi e v_F \boldsymbol{\sigma}, \quad (7)$$

so that the total current at each node is given by

$$\begin{aligned} \mathbf{J}_\chi &= \int d^3r \Psi_\chi^\dagger(\mathbf{r}) \mathbf{j}_\chi \Psi_\chi(\mathbf{r}) \\ &= -e\chi v_F \sum_{s,s',\mathbf{k}} [\eta_{\chi,s}^\dagger(\mathbf{k}) \boldsymbol{\sigma} \eta_{\chi,s'}(\mathbf{k})] c_{\chi,s,\mathbf{k}}^\dagger c_{\chi,s',\mathbf{k}}. \end{aligned} \quad (8)$$

The current operator enters the definition of the retarded current-current response tensor $\overleftrightarrow{\chi}_\chi^R(\omega)$ which is obtained by taking the analytic continuation $i\Omega_n \rightarrow \omega + i\delta$ of the two-particle Matsubara Green's function

$$\overleftrightarrow{\chi}_\chi(i\Omega_n) = -\frac{1}{V\hbar} \int_0^{\beta\hbar} d\tau \langle T \mathbf{J}_\chi(\tau) \mathbf{J}_\chi(0) \rangle e^{i\Omega_n \tau}, \quad (9)$$

where τ is the imaginary time, Ω_n is a bosonic Matsubara frequency and $\beta = 1/k_B T$ with k_B the Boltzmann constant. The optical conductivity tensor can then be calculated from the expression

$$\overleftrightarrow{\sigma}(\omega) = \frac{i}{\omega + i\delta} \sum_x [\overleftrightarrow{\chi}_\chi(\omega) - \overleftrightarrow{\chi}_\chi(0)]. \quad (10)$$

In the absence of an external static magnetic field and for the simple Hamiltonian given in Eq. (1), $\sigma_{i,j}(\omega) = \delta_{i,j} \sigma(\omega)$ so that we only need to compute the response function

$$\begin{aligned} \chi_\chi(\omega) &= -\frac{e^2 v_F^2}{\hbar V} \sum_{s,s',\mathbf{k}} \left| \eta_{\chi,s}^\dagger(\mathbf{k}) \sigma^{(\alpha)} \eta_{\chi,s'}(\mathbf{k}) \right|^2 \\ &\times \frac{\langle n_{\chi,s'}(\mathbf{k}) \rangle - \langle n_{\chi,s}(\mathbf{k}) \rangle}{\omega + i\delta - (E_{\chi,s'}(\mathbf{k}) - E_{\chi,s}(\mathbf{k}))/\hbar}, \end{aligned} \quad (11)$$

where $\langle n_{\chi,s}(\mathbf{k}) \rangle = \langle c_{\chi,s,\mathbf{k}}^\dagger c_{\chi,s,\mathbf{k}} \rangle$ is the average occupation of the state (χ, s, \mathbf{k}) at zero temperature and α can be any of x, y, z .

The relative dielectric tensor is

$$\varepsilon(\omega) = \varepsilon_b + \frac{i\sigma(\omega)}{\varepsilon_0(\omega + i\delta)}, \quad (12)$$

where ε_b is the bound charge contribution. We take $\varepsilon_b = 1$ in our calculations, but comment later on the effect of

a larger ε_b on the Kerr rotation. We assume that the two nodes are at a thermodynamical equilibrium with a Fermi level e_F so that the Fermi wave vector $k_{F,\chi}$ and the Fermi level $e_{F,\chi}$ for each node are related by

$$e_{F,\chi} = \hbar v_F k_{F,\chi} = e_F - \chi \hbar b_0. \quad (13)$$

The optical conductivity has contributions from the interband and intraband transitions. Both contributions have been calculated in parts in a number of papers^{13,14,18-21}. For completeness, we derive the intraband contribution in Appendix A. In the absence of magnetic field and in the continuum model, the relative dielectric function is

$$\begin{aligned} \varepsilon(\omega) &= 1 \\ &+ \gamma \sum_\chi \left[i\theta(\omega - 2v_F k_{F,\chi}) + \frac{1}{\pi} \ln \left(\frac{\omega^2 - 4v_F^2 k_c^2}{\omega^2 - 4v_F^2 k_{F,\chi}^2} \right) \right] \\ &+ \gamma \sum_\chi \frac{4}{\pi \hbar^2 \omega} \frac{i\tau}{1 + \omega^2 \tau^2} \left(e_{F,\chi}^2 + \frac{1}{3} \hbar^2 \omega^2 + \frac{\hbar^2}{4\tau^2} \right) \\ &- \gamma \sum_\chi \frac{4}{\pi \hbar^2} \frac{\tau^2}{1 + \omega^2 \tau^2} \left(e_{F,\chi}^2 - \frac{\hbar^2}{12\tau^2} \right), \end{aligned} \quad (14)$$

where $\gamma = \frac{\alpha}{6v_F/c}$, k_c is a cutoff wave vector which is related to the applicability of the linear dispersion relation and τ is the scattering time that enters in the calculation of the intraband conductivity (see Appendix A). The last two lines in Eq. (14) are intraband contributions to the dielectric function.

III. DIELECTRIC TENSOR OF A WSM IN A MAGNETIC FIELD

In a magnetic field $\mathbf{B} = \nabla \times \mathbf{A} = B\hat{z}$ and in the Landau gauge $\mathbf{A} = (0, Bx, 0)$, the single-particle Hamiltonian becomes, after making the Peierls substitution $\mathbf{k} \rightarrow \mathbf{k} + e\mathbf{A}/\hbar$,

$$h_\chi(\mathbf{k}) = \chi \hbar b_0 I_2 + \chi \hbar v_F \begin{pmatrix} k_z & \frac{\sqrt{2}}{\ell} a \\ \frac{\sqrt{2}}{\ell} a^\dagger & -k_z \end{pmatrix}, \quad (15)$$

where I_2 is the 2×2 unit matrix and the ladder operators are defined by

$$a = \frac{\ell}{\sqrt{2}\hbar} (P_x - iP_y), \quad (16)$$

$$a^\dagger = \frac{\ell}{\sqrt{2}\hbar} (P_x + iP_y), \quad (17)$$

where $\mathbf{P} \equiv \hbar\mathbf{k} + e\mathbf{A}$. They obey the commutation relation $[a, a^\dagger] = 1$. Here $h_\chi(\mathbf{k})$ is written in the same basis as that used in Eq. (1).

The energy spectrum of a Weyl node now consists of a *chiral* Landau level (index $n = 0$) which disperses in one

direction only according to

$$E_{\chi,0}(k) = \chi \frac{\hbar v_F}{\ell} \left(-k\ell + \frac{b_0\ell}{v_F} \right) \quad (18)$$

and of a set of positive and negative energy Landau levels $n = 1, 2, 3, \dots$ with dispersion

$$E_{\chi,n>0,s}(k) = \frac{\hbar v_F}{\ell} \left(s\sqrt{k^2\ell^2 + 2n} + \chi \frac{b_0\ell}{v_F} \right). \quad (19)$$

We use the index $s = +1(-1)$ for the Landau levels that originate from the conduction (valence) band of the Dirac cone and take $\hbar k$ as the momentum of the electron in the direction of the magnetic field. At some places in this paper, we use the alternative notation $n < 0$ for the Landau levels of the valence band. The corresponding eigenvectors are

$$v_{\chi,n,X,s}(k, \mathbf{r}) = \frac{1}{\sqrt{L_z}} e^{ikz} \eta_{\chi,n,X,s}(k, \mathbf{r}), \quad (20)$$

where L_z is the length of the WSM in the z direction and \mathbf{r} a two-dimensional vector in the plane perpendicular to z . The spinors are given by

$$\eta_{\chi,0,X}(k, \mathbf{r}) = \begin{pmatrix} 0 \\ h_{0,X}(\mathbf{r}) \end{pmatrix}, \quad (21)$$

for the chiral level and by

$$\eta_{\chi,n,X,s}(k, \mathbf{r}) = \begin{pmatrix} u_{\chi,n,s}(k) h_{n-1,X}(\mathbf{r}) \\ v_{\chi,n,s}(k) h_{n,X}(\mathbf{r}) \end{pmatrix} \quad (22)$$

for the others. We set $h_{n,X}(\mathbf{r}) = 0$ when $n < 0$. The u 's and v 's obey the normalization condition $|u_{\chi,n,s}(k)|^2 + |v_{\chi,n,s}(k)|^2 = 1$ and are given by

$$\begin{pmatrix} u_{\chi,n,s}(k) \\ v_{\chi,n,s}(k) \end{pmatrix} = \frac{1}{\sqrt{2}} \begin{pmatrix} -\chi s i \left(\sqrt{1 + \chi s \frac{k\ell}{e_n(k)}} \right) \\ \sqrt{1 - \chi s \frac{k\ell}{e_n(k)}} \end{pmatrix}, \quad (23)$$

where

$$e_n(k) = \sqrt{k^2\ell^2 + 2n}. \quad (24)$$

In Eq. (22), the functions $h_{n,X}(\mathbf{r}) = \frac{1}{\sqrt{L_y}} \varphi_n(x - X) e^{-iXy/\ell^2}$ are the Landau level wave functions in the Landau gauge with X the guiding-center index and the $\varphi_n(x)$'s are the wave functions of the one-dimensional harmonic oscillator. Each Landau level (χ, n, s, k) has degeneracy $N_\varphi = S/2\pi\ell^2$ where $\ell = \sqrt{\hbar/eB}$ is the magnetic length and $S = L_x L_y$ is the area of the WSM perpendicular to the magnetic field.

The field operator can now be written as

$$\Psi_\chi(\mathbf{r}, z) = \frac{1}{\sqrt{L_z}} \sum_{n,s,X,k} e^{ikz} \eta_{\chi,n,X,s}(k, \mathbf{r}) c_{\chi,n,X,s,k} \quad (25)$$

and the second quantized form of the current operator is

$$\mathbf{J}_\chi = \sum_{n,s,n',s',k} \sum_X \mathbf{\Gamma}_{\chi;ns;n's'}(k) c_{\chi,n,X,s,k}^\dagger c_{\chi,n',X,s',k}, \quad (26)$$

with the matrix elements defined by

$$\Gamma_{\chi;ns;n's'}^{(x)}(k) = -e\chi v_F \left[u_{\chi,n,s}^*(k) v_{\chi,n-1,s'}(k) \delta_{n-1,n} \right. \\ \left. + v_{\chi,n,s}^*(k) u_{\chi,n+1,s'}(k) \delta_{n,n'-1} \right]. \quad (27)$$

$$\Gamma_{\chi;ns;n's'}^{(y)}(k) = ie\chi v_F \left[u_{\chi,n,s}^*(k) v_{\chi,n-1,s'}(k) \delta_{n-1,n} \right. \\ \left. - v_{\chi,n,s}^*(k) u_{\chi,n+1,s'}(k) \delta_{n,n'-1} \right], \quad (28)$$

$$\Gamma_{\chi;ns;n's'}^{(z)}(k) = -e\chi v_F \left[u_{\chi,n,s}^*(k) u_{\chi,n,s'}(k) \right. \\ \left. - v_{\chi,n,s}^*(k) v_{\chi,n,s'}(k) \right] \delta_{n,n'}. \quad (29)$$

The current-current response tensor defined in Eq. (9) becomes

$$\chi_{\chi,(\alpha,\beta)}(\omega) = \zeta \sum_{\substack{k,n,n', \\ s,s'}} \Gamma_{\chi;n,s;n',s'}^{(\alpha)}(k) \Gamma_{\chi;n',s';n,s}^{(\beta)}(k) \\ \times \frac{\langle n_{\chi,n',s'}(k) \rangle - \langle n_{\chi,n,s}(k) \rangle}{\omega + i\delta - (E_{\chi,n's'}(k) - E_{\chi,n,s}(k))/\hbar}, \quad (30)$$

where $\zeta = -1/2\pi\ell^2\hbar L_z$, with L_z the width of the WSM in the z direction. The filling factor for each Landau level is given by

$$\langle n_{\chi,n,s}(k) \rangle = \frac{1}{N_\varphi} \sum_X \left\langle c_{\chi,n,X,s,k}^\dagger c_{\chi,n,X,s,k} \right\rangle. \quad (31)$$

The conductivity tensor is obtained from Eq. (10) and the relative dielectric tensor from Eq. (12).

The response functions $\chi_{\chi,(\alpha,z)}$ and $\chi_{\chi,(z,\alpha)}$ with $\alpha = x, y$ are zero because of the Kronecker deltas in the matrix elements $\mathbf{\Gamma}_{\chi;ns;n's'}$. Moreover, for the interband part of the response functions (i.e., $s \neq s'$), we have the symmetry relations $\chi_{\chi,(x,x)} = \chi_{\chi,(y,y)}$ and $\chi_{\chi,(x,y)} = -\chi_{\chi,(y,x)}$. The optical selection rules imposed by the matrix elements are such that only the dipolar transitions $|n| = |n| \pm 1$ (here $n = 0, \pm 1, \pm 2, \dots$) are permitted in $\chi_{\chi,(\alpha,\beta)}$ with $\alpha, \beta = x, y$ while only the transitions $-n \rightarrow n$ are permitted in $\chi_{\chi,(z,z)}$. (A tilt of a Weyl cone allows for a much richer interband spectrum^{15,22}). We limit our study to the ultra-quantum regime where the Fermi level lies in the chiral level. In this case, intraband transitions can only occur in level $n = 0$ and they contribute only to $\chi_{\chi,(z,z)}$. The calculation of the dynamic conductivity tensor including inter- and intra-Landau-level contributions is summarized in Appendix B.

IV. MAXWELL EQUATIONS WITH THE AXION TERMS

To compute the optical properties of a WSM, we must take into account the modification of the Maxwell equations by the topological axion term $\theta(\mathbf{r}, t) = 2\mathbf{b} \cdot \mathbf{r} - 2b_0 t$.

The modified equations are¹²:

$$\nabla \cdot \mathbf{D} = \rho_f + \kappa \sqrt{\frac{\varepsilon_0}{\mu_0}} \mathbf{b} \cdot \mathbf{B}, \quad (32)$$

$$\nabla \cdot \mathbf{B} = 0, \quad (33)$$

$$\nabla \times \mathbf{E} = -\frac{\partial \mathbf{B}}{\partial t}, \quad (34)$$

$$\nabla \times \mathbf{H} = \frac{\partial \mathbf{D}}{\partial t} + \mathbf{J}_f - \kappa \sqrt{\frac{\varepsilon_0}{\mu_0}} (\mathbf{b} \times \mathbf{E} - gb_0 \mathbf{B}), \quad (35)$$

where $\kappa = 2\alpha/\pi$ with α the fine-structure constant. In these equations, ρ_f is the free (or induced) charge density and $\mathbf{J}_f = \overleftrightarrow{\sigma} \cdot \mathbf{E}$ is the induced current density with $\overleftrightarrow{\sigma}$ the conductivity tensor for the two-node model calculated in appendices A and B. In this paper, we assume that the relative permeability $\mu_r = \mu/\mu_0$ is unity.

In the context of the chiral magnetic effect which occurs in the nonequilibrium condition where the chiral chemical potentials of both nodes are different, the last term in the Ampere-Maxwell equation has $g = 1$. In this paper, however, we have a different situation since we assume that the two nodes are at equilibrium and that the two Dirac points are separated in energy by $2\hbar b_0$. The extra current $gb_0 \mathbf{B}$ is then related to the natural optical activity of the WSM and it follows that $g = 1/3$ in the dynamic case and $g = 0$ in the static case²³ and ²⁴. The gyrotropic effect of b_0 is, as we will show, very small in comparison with that of axion term \mathbf{b} so that, in the THz frequency range where we study the Kerr rotation, taking $g = 1$ or $g = 1/3$ or even $g = 0$ does not make any numerical difference to the results presented in this paper. In the small frequency limit, however, keeping g finite as $\omega \rightarrow 0$ leads to some strange results as we will point out at some places in this paper.

The wave equation in the presence of the axion terms can be written in the matrix form $M_{i,j}E_j = 0$ where the components of the matrix M are given by

$$M_{ij} = -c^2 (q^2 \delta_{ij} - q_i q_j) + \omega^2 \tilde{\varepsilon}_{ij}, \quad (36)$$

where δ_{ij} is the Kronecker delta. We have defined the tensor $\tilde{\varepsilon}_{ij}$ by

$$\tilde{\varepsilon}_{ij} = \varepsilon_{ij} + \frac{i}{\omega} c \kappa \varepsilon_{ijk} \left(b_k - \frac{gb_0}{\omega} q_k \right), \quad (37)$$

with ε_{ijk} the antisymmetric Levi-Civita tensor and the components of the dielectric tensor ε_{ij} are given by

$$\varepsilon_{ij} = \varepsilon_b \delta_{ij} + \frac{i}{\varepsilon_0 \omega} \sigma_{ij}, \quad (38)$$

where the electrons in each node are described by the hamiltonian of Eq. (1) or Eq. (15) which contains the axion term b_0 but not \mathbf{b} . In Eq. (38), ε_b is the effective background dielectric constant. We take $\varepsilon_b = 1$, but it must be kept in mind that ε_b can be substantially larger in WSMs. For example $\varepsilon_b = 6.2$ in type-I WSM TaAs²⁵.

The dispersion relations and polarizations of the electromagnetic modes are obtained from the equations

$\det[M] = 0$ and $M_{i,j}E_j = 0$ respectively. We stress once again that in the continuum model that we use, the axion term b_0 is present in the dielectric tensor $\overleftrightarrow{\varepsilon}$ and in the Maxwell equations but the axion term \mathbf{b} appears in the modified Maxwell equations but not in $\overleftrightarrow{\varepsilon}$. The induced charge density, if any, is given by

$$\rho_f = i\varepsilon_0 \mathbf{q} \cdot (\tilde{\varepsilon} \cdot \mathbf{E}). \quad (39)$$

V. KERR AND ELLIPTICITY ANGLES

In this section, we derive the formulas necessary to compute the Kerr and ellipticity angles. The external magnetic field, when present, is set along the z direction and we restrict our analysis to the case where the axion term $\mathbf{b} = \mathbf{b}_{\parallel} = b_z \hat{\mathbf{z}}$. We study the effect of $\mathbf{b}_{\perp} = b_x \hat{\mathbf{x}} + b_y \hat{\mathbf{y}}$ in Sec. IX.

We consider a linearly polarized electromagnetic wave with amplitude E_0 , polarization \mathbf{e}_0 and wave vector \mathbf{q}_0 arriving at normal incidence on the surface of a semi-infinite WSM either along the z axis with $\mathbf{e}_0 \perp \mathbf{B}$ (the Faraday configuration) or along the x axis with $\mathbf{e}_0 \cdot \mathbf{B} \neq 0$ (the Voigt configuration)¹⁷. If $\mathbf{B} = 0$, we use the name Faraday configuration for $\mathbf{e}_0 \perp \mathbf{b}$ and Voigt configuration for $\mathbf{e}_0 \cdot \mathbf{b} \neq 0$

A. Faraday configuration

In the Faraday configuration, the vacuum (medium 1)-WSM (medium 2) interface is at $z = 0$. The electromagnetic field in medium 1 (with dispersion $q_0 = \omega/c$) is given by

$$\mathbf{E}_1(z,t) = E_0 \mathbf{e}_0 e^{iq_0 z} e^{-i\omega t} + E_0 r \mathbf{e}_r e^{-iq_0 z} e^{-i\omega t}, \quad (40)$$

$$\mathbf{B}_1(z,t) = \frac{q_0}{\omega} E_0 (\hat{\mathbf{z}} \times \mathbf{e}_0) e^{iq_0 z} e^{-i\omega t} - \frac{q_0}{\omega} E_0 r (\hat{\mathbf{z}} \times \mathbf{e}_r) e^{-iq_0 z} e^{-i\omega t}, \quad (41)$$

while in medium 2, the two transmitted waves with wave vector q_1 and q_2 are given by

$$\mathbf{E}_2(z,t) = E_0 t_1 \mathbf{e}_1 e^{iq_1 z} e^{-i\omega t} + E_0 t_2 \mathbf{e}_2 e^{iq_2 z} e^{-i\omega t}, \quad (42)$$

$$\mathbf{B}_2(z,t) = \frac{q_1}{\omega} E_0 t_1 (\hat{\mathbf{z}} \times \mathbf{e}_1) e^{iq_1 z} e^{-i\omega t} + \frac{q_2}{\omega} E_0 t_2 (\hat{\mathbf{z}} \times \mathbf{e}_2) e^{iq_2 z} e^{-i\omega t}. \quad (43)$$

In these equations, $\mathbf{e}_0, \mathbf{e}_r, \mathbf{e}_1, \mathbf{e}_2$ are the (complex) polarization vectors for the incoming, reflected and transmitted waves respectively and r, t_1, t_2 are the reflection and transmission factors.

At the surface of the WSM, the electric and magnetic

fields must satisfy the boundary conditions

$$(\mathbf{D}_1 - \mathbf{D}_2) \cdot \hat{\mathbf{n}} = \rho_{free}, \quad (44)$$

$$\mathbf{E}_{1,\parallel} - \mathbf{E}_{2,\parallel} = 0, \quad (45)$$

$$(\mathbf{B}_1 - \mathbf{B}_2) \cdot \hat{\mathbf{n}} = 0, \quad (46)$$

$$\mathbf{B}_{1,\parallel} - \mathbf{B}_{2,\parallel} = 0, \quad (47)$$

where the unit vector $\hat{\mathbf{n}}$ points from medium 2 to medium 1.

Defining the complex polarization vectors by

$$\mathbf{e}_j = \alpha_j \hat{\mathbf{x}} + \beta_j \hat{\mathbf{y}}, \quad (48)$$

with $j = 0, r, 1, 2$ (a polarization component along z , if any, does not contribute to the boundary conditions), we get from Eqs. (44)-(47) the system of equations

$$\begin{pmatrix} r\alpha_r \\ r\beta_r \\ t_1 \\ t_2 \end{pmatrix} = \begin{pmatrix} 1 & 0 & -\alpha_1 & -\alpha_2 \\ 0 & 1 & -\beta_1 & -\beta_2 \\ 0 & 1 & \frac{q_1}{q_i}\beta_1 & \frac{q_2}{q_i}\beta_2 \\ -1 & 0 & -\frac{q_1}{q_i}\alpha_1 & -\frac{q_2}{q_i}\alpha_2 \end{pmatrix}^{-1} \begin{pmatrix} -\alpha_0 \\ -\beta_0 \\ \beta_0 \\ -\alpha_0 \end{pmatrix}. \quad (49)$$

In the Faraday configuration, the WSM has rotational symmetry along the z axis since both \mathbf{b} and \mathbf{B} are along that axis, and we can take without loss of generality $\mathbf{e}_0 = \hat{\mathbf{x}}$ for the incident linear polarization. This choice implies $\alpha_i = 1, \beta_i = 0$ and the reflection and transmission factors are then given by

$$r\alpha_r = \frac{\left(1 - \frac{q_1}{q_0}\right) \left(1 + \frac{q_2}{q_0}\right) \alpha_1 \beta_2 - \left(1 + \frac{q_1}{q_0}\right) \left(1 - \frac{q_2}{q_0}\right) \alpha_2 \beta_1}{\left(\frac{q_1}{q_0} + 1\right) \left(\frac{q_2}{q_0} + 1\right) (\alpha_1 \beta_2 - \alpha_2 \beta_1)} \quad (50)$$

and

$$r\beta_r = -2 \frac{\left(\frac{q_1}{q_0} - \frac{q_2}{q_0}\right) \beta_1 \beta_2}{\left(\frac{q_1}{q_0} + 1\right) \left(\frac{q_2}{q_0} + 1\right) (\alpha_1 \beta_2 - \alpha_2 \beta_1)}. \quad (51)$$

With $b_0, b_z \neq 0$, the matrix M takes the block-diagonal form

$$M = \begin{pmatrix} \omega^2 \tilde{\varepsilon}_{xx} - c^2 q^2 & \omega^2 \tilde{\varepsilon}_{xy} & 0 \\ -\omega^2 \tilde{\varepsilon}_{xy} & \omega^2 \tilde{\varepsilon}_{xx} - c^2 q^2 & 0 \\ 0 & 0 & \omega^2 \tilde{\varepsilon}_{zz} \end{pmatrix}. \quad (52)$$

The dispersion relations of the electromagnetic waves are then given by (the same dispersions are obtained in Refs. 26 and 27)

$$q_{1,\pm} = -\frac{g\kappa b_0}{2c} \pm \sqrt{\left(\frac{g\kappa b_0}{2c}\right)^2 + \frac{\omega^2 \xi_-}{c^2}}, \quad (53)$$

$$q_{2,\pm} = \frac{g\kappa b_0}{2c} \pm \sqrt{\left(\frac{g\kappa b_0}{2c}\right)^2 + \frac{\omega^2 \xi_+}{c^2}}, \quad (54)$$

where we have defined the functions

$$\xi_{\pm} = \varepsilon_{xx} \pm i\varepsilon_{xy} \mp \frac{c\kappa b_z}{\omega}. \quad (55)$$

The corresponding polarizations are given by

$$\mathbf{e}_{1,\pm} = \frac{1}{\sqrt{2}} \begin{pmatrix} i \\ 1 \\ 0 \end{pmatrix}; \quad \mathbf{e}_{2,\pm} = \frac{1}{\sqrt{2}} \begin{pmatrix} -i \\ 1 \\ 0 \end{pmatrix}, \quad (56)$$

while for the plasmon mode defined by $\varepsilon_{zz} = 0$, we have

$$\mathbf{e}_3 = \begin{pmatrix} 0 \\ 0 \\ 1 \end{pmatrix}. \quad (57)$$

The polarization vectors show that both the magnetic field (if present) and the axion terms b_0, b_z lead to circular birefringence.

In deriving Eq. (49), we have implicitly assumed that there are only two electromagnetic modes propagating in each direction. This is not obvious from the dispersions given by Eqs. (50) and (51) when $b_0 \neq 0$. We did check numerically, however, that such was the case for the results presented in this paper.

From $\mathbf{e}_{1,+}$ and $\mathbf{e}_{2,+}$, we get $\alpha_1 = -\alpha_2 = i/\sqrt{2}$ and $\beta_1 = \beta_2 = 1/\sqrt{2}$ for the parameters in Eqs. (50) and (51). To compute the Kerr angle, we first define a function η by

$$\eta = \frac{r\beta_r}{r\alpha_r} = \frac{i \left(\frac{q_{1,+}}{q_0} - \frac{q_{2,+}}{q_0} \right)}{1 - \frac{q_{1,+} + q_{2,+}}{q_0}}. \quad (58)$$

In all our numerical results, we have checked by plotting the dispersions that $q_{1,+}$ and $q_{2,+}$ always have positive real and imaginary parts in the frequency range considered.

If $g = 0$ in the M , matrix (but b_0 is present in the conductivity tensor), Eq. (58) reduces to the simpler form

$$\eta = \frac{r\beta_r}{r\alpha_r} = \frac{i(\sqrt{\xi_-} - \sqrt{\xi_+})}{1 - \sqrt{\xi_- \xi_+}}. \quad (59)$$

In the general case where the polarization of the reflected wave is elliptical, the Kerr angle θ_K is defined as the angle that the major axis of the polarization ellipse makes with the direction of the incident (linear) polarization i.e., the x axis if $\mathbf{e}_0 = \hat{\mathbf{x}}$. We use the definition²⁸

$$\tan 2\theta_K = \frac{2 \operatorname{Re}[\eta]}{1 - |\eta|^2}, \quad (60)$$

where $\theta_K \in [-\pi/2, \pi/2]$.

The major and minor axis of the ellipse have length a and d respectively. The ellipticity angle ψ_K is defined²⁸ as

$$\tan \psi_K = \pm \frac{d}{a}, \quad (61)$$

where the \pm signs indicate the direction of rotation of the electric field vector along the ellipse and $d/a \in [0, 1]$.

Thus, a change in the sign of the ellipticity corresponds to a change in the direction of the rotation of the electric field vector on the ellipse. The ellipticity angle is obtained from the equation

$$\sin 2\psi_K = \frac{2 \operatorname{Im}[\eta]}{1 + |\eta|^2}. \quad (62)$$

A linear polarization has $\psi_K = 0$ while a purely circular polarization has $\psi_K = \pi/4$. In the case of a WSM, $|\eta|$ is generally not small so that approximate formulas with $|\eta| = 0$ in the denominator of Eqs. (60) and (62) cannot be used. We remark that, when $\operatorname{Re}[\eta] = 0$, $\theta_K = 0$ if $1 - |\eta|^2 > 0$ but $\theta_K = \pi/2$ if $1 - |\eta|^2 < 0$. An abrupt $\pi/2$ rotation of the Kerr angle is thus possible when $1 - |\eta|^2$ changes sign with a small variation of ω or B .

B. Voigt configuration

In the Voigt configuration, the incident wave propagates along the x axis with the magnetic field along the z axis. The analysis proceeds as in the Faraday case but with z replaced by x in Eqs. (40)-(43) and with the polarization vectors of Eq. (48) now defined by

$$\mathbf{e}_j = \alpha_j \hat{\mathbf{z}} + \beta_j \hat{\mathbf{y}}. \quad (63)$$

(A polarization component along x , if present, does not contribute to the boundary conditions.) The reflection and transmission factors are still given by Eq. (49). In this configuration, it is necessary to take the incident polarization at an angle with respect to the y or z axis in order to get a Kerr rotation¹⁷. We choose for the incident polarization $\mathbf{e}_0 = 1/\sqrt{2}(\hat{\mathbf{y}} + \hat{\mathbf{z}})$ and so we get

$$r\alpha_r = \frac{1}{\sqrt{2}} \frac{\left(1 - \frac{q_1 q_2}{q_0^2}\right)}{\left(\frac{q_1}{q_0} + 1\right) \left(\frac{q_2}{q_0} + 1\right)} \quad (64)$$

$$- \frac{1}{\sqrt{2}} \frac{\left(\frac{q_1}{q_0} - \frac{q_2}{q_0}\right) (\alpha_1 \beta_2 + \alpha_2 \beta_1 - 2\alpha_1 \alpha_2)}{\left(\frac{q_1}{q_0} + 1\right) \left(\frac{q_2}{q_0} + 1\right) (\alpha_1 \beta_2 - \alpha_2 \beta_1)}$$

and

$$r\beta_r = \frac{1}{\sqrt{2}} \frac{\left(1 - \frac{q_1 q_2}{q_0^2}\right)}{\left(\frac{q_1}{q_0} + 1\right) \left(\frac{q_2}{q_0} + 1\right)} \quad (65)$$

$$+ \frac{1}{\sqrt{2}} \frac{\left(\frac{q_1}{q_0} - \frac{q_2}{q_0}\right) (\alpha_1 \beta_2 + \alpha_2 \beta_1 - 2\beta_1 \beta_2)}{\left(\frac{q_1}{q_0} + 1\right) \left(\frac{q_2}{q_0} + 1\right) (\alpha_1 \beta_2 - \alpha_2 \beta_1)}.$$

In this configuration, the M matrix with $b_0, b_z \neq 0$ is given by

$$M = \begin{pmatrix} \omega^2 \varepsilon_{xx} & \omega^2 \bar{\varepsilon}_{xy} & 0 \\ -\omega^2 \bar{\varepsilon}_{xy} & \omega^2 \varepsilon_{xx} - c^2 q^2 & -i\kappa g b_0 q \\ 0 & i\kappa g b_0 q & \omega^2 \varepsilon_{zz} - c^2 q^2 \end{pmatrix}, \quad (66)$$

where the function

$$\bar{\varepsilon}_{xy} = \varepsilon_{xy} + i \frac{c\kappa b_z}{\omega}. \quad (67)$$

The dispersion relations of the electromagnetic waves are given by

$$q_i = \pm \frac{\omega}{c} \sqrt{\frac{\varepsilon_W \pm \sqrt{\varepsilon_W^2 - 4\varepsilon_V \varepsilon_{zz}}}{2}}, \quad (68)$$

where we have defined the dielectric functions

$$\varepsilon_V = \varepsilon_{xx} + \frac{\bar{\varepsilon}_{xy}^2}{\varepsilon_{xx}}, \quad (69)$$

$$\varepsilon_W = \varepsilon_V + \varepsilon_{zz} + \frac{\kappa^2 g^2 b_0^2}{\omega^2}. \quad (70)$$

The function ε_V is the so-called Voigt dielectric function¹⁷. The four corresponding eigenvectors are then (when $\omega^2 \varepsilon_{zz} - c^2 q_i^2 \neq 0, \varepsilon_{xx} \neq 0, b_0 \neq 0$)

$$\mathbf{e}_i = \frac{1}{\Lambda_i(q)} \begin{pmatrix} -\frac{\bar{\varepsilon}_{xy}}{\varepsilon_{xx}} \\ 1 \\ \frac{-i\kappa g b_0 c q_i}{\omega^2 \varepsilon_{zz} - c^2 q_i^2} \end{pmatrix}, \quad (71)$$

with the normalization condition

$$\Lambda(q_i) = \sqrt{1 + \left|\frac{\bar{\varepsilon}_{xy}}{\varepsilon_{xx}}\right|^2 + \left|\frac{\kappa g b_0 c q_i}{\omega^2 \varepsilon_{zz} - c^2 q_i^2}\right|^2}. \quad (72)$$

The wave vector q_i in Eqs. (71)-(72) is one of the four combinations given by Eq. (68). A particularity of the Voigt configuration is that there is a component of the polarization vector along the direction of propagation of the wave. It is given by

$$E_x = -\frac{\bar{\varepsilon}_{xy}}{\varepsilon_{xx}} E_y. \quad (73)$$

From the polarization vectors, we have for the function η the expression

$$\eta = \frac{(\alpha_1 - \alpha_2) \left(1 - \frac{q_1 q_2}{q_0^2}\right) + (\alpha_1 + \alpha_2 - 2) \left(\frac{q_1}{q_0} - \frac{q_2}{q_0}\right)}{(\alpha_1 - \alpha_2) \left(1 - \frac{q_1 q_2}{q_0^2}\right) - (\alpha_1 + \alpha_2 - 2\alpha_1 \alpha_2) \left(\frac{q_1}{q_0} - \frac{q_2}{q_0}\right)}, \quad (74)$$

where

$$\alpha_i = \frac{-i\kappa g b_0 c q_i}{\omega^2 \varepsilon_{zz} - c^2 q_i^2}, \quad (75)$$

where $i = 1, 2$ and q_1, q_2 are the two wave vectors of Eq. (68) propagating in the positive x direction.

The M matrix becomes block diagonal and the analysis simplifies considerably if $g = 0$ in the matrix M . The four dispersions are then given by

$$q_{1,\pm} = \pm \frac{\omega}{c} \sqrt{\varepsilon_V}, \quad (76)$$

$$q_{2,\pm} = \pm \frac{\omega}{c} \sqrt{\varepsilon_{zz}}, \quad (77)$$

with the eigenvectors

$$\mathbf{e}_{1,\pm} = \frac{1}{\sqrt{|\varepsilon_{xx}|^2 + |\bar{\varepsilon}_{xy}|^2}} \begin{pmatrix} -\bar{\varepsilon}_{xy} \\ \varepsilon_{xx} \\ 0 \end{pmatrix}, \quad (78)$$

and

$$\mathbf{e}_{2,\pm} = \begin{pmatrix} 0 \\ 0 \\ 1 \end{pmatrix}. \quad (79)$$

The polarization vectors give $\beta_1 = \varepsilon_{xx}/\sqrt{|\varepsilon_{xx}|^2 + |\bar{\varepsilon}_{xy}|^2}$, $\beta_2 = 0$ and $\alpha_1 = 0$, $\alpha_2 = 1$. Using these values in Eq. (49) with $\mathbf{e}_0 = \hat{\mathbf{y}}$ or $\mathbf{e}_0 = \hat{\mathbf{z}}$ gives zero Kerr rotation thus showing that it is necessary for the incident polarization to make an angle with the y or z axis in order to get a non-zero result. For the function η , we have

$$\eta = \frac{(1 - \sqrt{\varepsilon_V})(1 + \sqrt{\varepsilon_{zz}})}{(1 + \sqrt{\varepsilon_V})(1 - \sqrt{\varepsilon_{zz}})}. \quad (80)$$

The Kerr and ellipticity angles are given by Eq. (60) and (62). In Eq. (60), however, the angle is measured with respect to the z axis although the real rotation angle is that measured with respect to the incident polarization vector i.e., $\theta_K - \pi/4$.

VI. KERR ROTATION IN A NON TOPOLOGICAL METAL

For comparison with our results for a WSM, we give in this section the Kerr angle for an ordinary (non topological) metal. In this case, the conductivity tensor that enters the M matrix is given by

$$\sigma = i\varepsilon_0\omega_p^2\tau \begin{pmatrix} \frac{\omega\tau+i}{(\omega\tau+i)^2-(\omega_c\tau)^2} & \frac{-i\omega_c\tau}{(\omega\tau+i)^2-(\omega_c\tau)^2} & 0 \\ \frac{i\omega_c\tau}{(\omega\tau+i)^2-(\omega_c\tau)^2} & \frac{\omega\tau+i}{(\omega\tau+i)^2-(\omega_c\tau)^2} & 0 \\ 0 & 0 & \frac{1}{\omega\tau+i} \end{pmatrix}, \quad (81)$$

where the magnetic field $\mathbf{B} = B\hat{\mathbf{z}}$, τ is the transport scattering time, $\omega_c = eB/m_e$ the cyclotron frequency (with m_e the electron mass) and $\omega_p = \sqrt{n_e e^2/m_e \varepsilon_0}$ (with n_e the electronic density) is the plasmon frequency given by $\varepsilon_{zz}(\omega_p) = 0$. For an ordinary metal, $b_0 = 0$ and $\mathbf{b} = 0$.

In the Faraday configuration, the dispersions, polarizations and function η are given by Eqs. (53) and (54) and Eqs. (56) and (59). With a density $n_e \approx 10^{29} \text{ m}^{-3}$, and relaxation time $\tau \approx 10^{-14} \text{ s}$, we get $\omega_p\tau \approx 178 \text{ rad/s}$ and $\omega_c\tau \approx 1.8 \times 10^{-3} B$ with B in Tesla. Figure 1 shows that, in the optical frequency range the Kerr and ellipticity angles are extremely small. (The peak in θ_K occurs at the plasmon frequency in the ultraviolet frequency domain). If the density is decreased to $n_e \approx 10^{23} \text{ m}^{-3}$ (a value closer to what can be found in a WSM), the Kerr

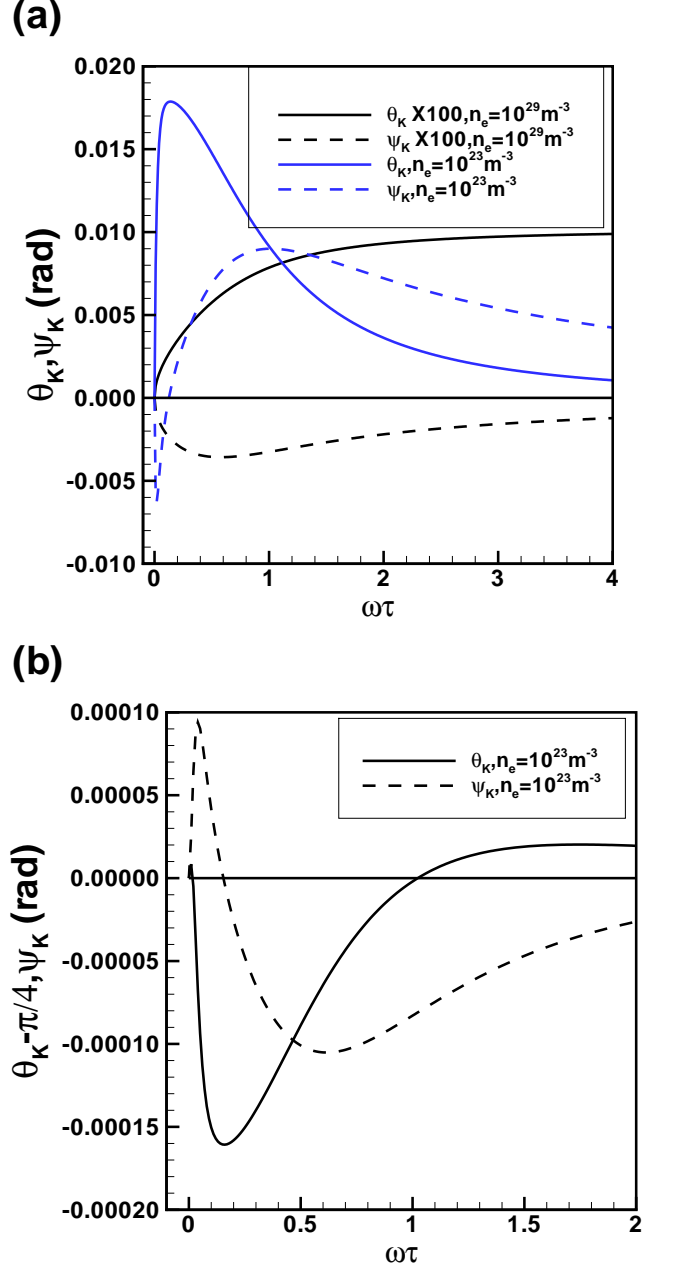


FIG. 1. Frequency behavior of the Kerr and ellipticity angles θ_K, ψ_K in the (a) Faraday and (b) Voigt configuration for an ordinary (non topological) metal in a magnetic field. Parameters: $\tau = 10^{-14} \text{ s}$, $B = 10 \text{ T}$, $\omega_c\tau = 0.0178$ and $\omega_p\tau = 178$ (if $n_e = 10^{29} \text{ m}^{-3}$), $\omega_p\tau = 0.178$ (if $n_e = 10^{23} \text{ m}^{-3}$).

and ellipticity angles are substantially increased. Equation (59) shows that the Kerr angle changes sign if the direction of the magnetic field is reversed.

In the Voigt configuration, the dispersions, polarizations and function η are given by Eqs. (76) and (79) and Eq. (80) respectively. For $n_e = 10^{29} \text{ m}^{-3}$, the Kerr ($\theta_K - \pi/4$) and ellipticity angles are virtually zero ($< 10^{-10} \text{ rad}$). For $n_e = 10^{22} \text{ m}^{-3}$, both angles are sub-

stantially bigger but much smaller than in the Faraday configuration for the same density. Since ε_V is even in B , the Kerr angle does not change sign if the magnetic field is reversed. A particularity of that configuration is that in the $q_{1,\pm}$ modes, $E_x = -\frac{\varepsilon_{xy}}{\varepsilon_{xx}}E_y$, so that there is a component of the polarization along the direction of propagation. There is, however, from Eq. (39), no induced charge.

The frequency profile $\theta_K(\omega)$ depends very much on the relative value of ω_p and ω_c . Values of these parameters other than those considered in this section are considered in Ref. 15.

VII. KERR ROTATION IN A WSM IN ZERO B FIELD

We proceed to the study the frequency behavior of the Kerr and ellipticity angles in a WSM in the absence of a magnetic field thus complementing earlier works^{13,14} on this subject. We limit our analysis to the case $b_0, b_z \neq 0$. We discuss the effect of \mathbf{b}_\perp in Sec. IX.

We take the wave vector k and the axion term b_z in units of $k_a = 10^8 \text{ m}^{-1}$ and choose $\hbar v_F k_a = 19.7 \text{ meV}$ with $v_F = 3 \times 10^5 \text{ m/s}$ as our energy unit ($v_F k_a = 3 \times 10^{13} \text{ s}^{-1}$). In the presentation of our results, we use the dimensionless variables $b_{0,r}, b_{z,r}, k_{c,r}, \omega_r, k_{F,\chi,r}$ which we define by

$$b_z = b_{z,r} k_a, k_c = k_{c,r} k_a, \quad (82)$$

$$b_0 = b_{0,r} v_F k_a, e_F = e_{F,r} \hbar v_F k_a, \quad (83)$$

$$k_{F,\chi} = k_{F,\chi,r} k_a, \omega = \omega_r v_F k_a. \quad (84)$$

We take these parameters in the range $\hbar b_0, e_F \in [0, 10] \text{ meV}$ and $b_z \in [-5 \times 10^8, 5 \times 10^8] \text{ m}^{-1}$, consistent with typical values reported in the literature^{29,30} (for example, $b = 3.2 \times 10^8 \text{ m}^{-1}$ in WTe_2 ³¹ and $v_F \approx 10^6 \text{ m/s}$). In our dimensionless units, these values correspond to $b_{0,r}, e_{F,r} \in [0, 0.5]$ and $b_{z,r} \in [-5, 5]$. We take $\tau = 10 \text{ ps}$ for the intranode scattering time (the internode scattering time requires a large momentum transfer and is substantially bigger^{7,32}). We take for the cutoff wave vector $k_{c,r} \approx 1000$. The numerical values of the Kerr angle, the position of its maximum, etc. all depend on the precise choice of k_c , but not the qualitative aspects of frequency profile $\theta_K(\omega)$.

A. Faraday configuration

In the Faraday configuration, the dispersions are obtained by setting $\varepsilon_{ij} = \varepsilon \delta_{ij}$ in Eq. (37). The dispersion relations, polarization and function η are given by Eqs. (53) and (54) and Eqs. (56) and (58) respectively but with ξ_\pm of Eq. (55) replaced by $\xi_\pm(\omega) = \varepsilon(\omega) \mp c\kappa b_z/\omega$.

The Kerr and ellipticity angles are shown in Fig. 2 for the case where we artificially set $b_z = e_F = 0$ in order to see the gyrotropic effect of b_0 alone. In this situation,

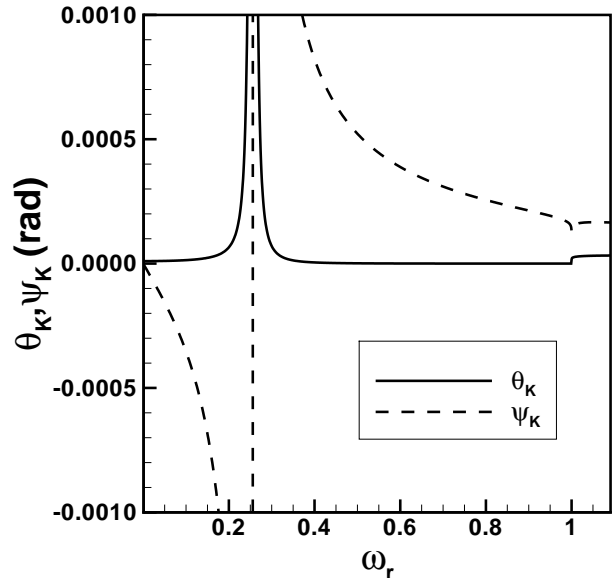


FIG. 2. Effect of the parameter $b_{0,r}$ alone on the frequency behavior of the Kerr and ellipticity angles in the Faraday configuration for a Weyl semimetal in zero magnetic field. Parameters are $\tau = 10 \text{ ps}$, $e_{F,r} = b_{z,r} = 0$, $b_{0,r} = 0.5$, $\mathbf{b}_\perp = 0$. The maximum of the Kerr angle (not shown) is 0.06 rad.

there is an equal number of electrons and holes but the WSM is at equilibrium. As can be seen from Fig. 2, the gyrotropic effect of b_0 is very small with the exception of a narrow peak at a frequency ω where $\varepsilon(\omega) = 0$ i.e., at the plasmon frequency^{33,34}. The ellipticity is also very small and changes sign at the plasmon frequency. The Kerr angle is positive for $b_0 > 0$, odd in b_0 and increases with $|b_0|$.

Because of the Pauli blocking, the frequency threshold $\omega_{th,r}$ for the electromagnetic absorption in each node is given by

$$\omega_{th,r} = 2|e_{F,r} - \chi b_{0,r}|. \quad (85)$$

Figure 2 shows that the Kerr angle has a step at this threshold which is at $\omega_r = 2b_{0,r} = 1$.

The dispersion relations in the Faraday configuration (Eqs. (53) and (54), contain both b_0 and b_z in the ratio

$$\frac{\omega^2 \frac{c\kappa b_z}{e^2} \omega}{\left(\frac{\kappa b_0}{2c}\right)^2} = \frac{4c\omega b_z}{\kappa b_0^2} = \frac{4\omega_r b_{z,r}}{\kappa b_{0,r}^2 v_{F,r}} \approx 10^6, \quad (86)$$

for $b_{z,r} = b_{0,r} = 1$, $v_{F,r} = 0.001$ and $\omega_r = 1$. Thus, in the THz frequency range, the gyrotropic effect of b_0 is negligible in comparison with that of b_z . This is also true in the Voigt configuration although the dispersion relations are more complex to analyze in this case.

Figure 3 shows the effect of b_z on θ_K and ψ_K when $b_0 = e_F = 0$. Although there is no carriers in this case, the Kerr angle is not zero because of the presence of b_z in

ξ_{\pm} . With our sign convention, θ_K is positive for negative b_z and vice-versa i.e., the Kerr effect is odd in b_z as reported previously¹⁴. Increasing $|b_z|$ does not change the maximal value ($\theta_{K,\max} \approx 0.5$ rad at $\omega_{\max,r}$) but broadens the frequency range where the Kerr angle is important and blueshifts the maximum. The Kerr angle is large in comparison with that due to b_0 alone or to that in a normal metal (see Fig. 1). When $b_0 = 0$, the Kerr angle is even in e_F so that electrons and holes contribute the same way to the Kerr rotation. Consequently, the Kerr angle is not zero at compensation when $e_F = 0$ and $b_0 \neq 0$.

In panel (a) of Fig. 3, the background dielectric constant is $\varepsilon_b = 1$. Since ε_b can be much larger in a WSM, we plot in panel (b) the same curves but for $\varepsilon_b = 10$. We see that the maximum value of the Kerr angle is unchanged as well as the overall profile of the curves which are only compressed and pushed to lower frequencies. At larger frequencies, the Kerr angle is reduced by a factor $\approx \varepsilon_b$.

Figure 4 shows the effect of b_z on the Kerr angle for finite b_0 and e_F . The threshold frequencies (which are independent of b_z) for the absorption given by Eq. (85) lead to two spikes in $\theta_K(\omega)$. Figure 4 shows how $\theta_K(\omega)$ changes when the two threshold frequencies are on the left, in the middle, and on the right of the frequency $\omega_{\max,r}$ where the Kerr angle is maximal. An interesting situation occurs when the two frequencies are on the right of the maximum in θ_K . In this case, the Kerr angle takes its maximal value $\theta_{K,\max} = \pi/2$ and a plateau where $\theta_K = 0$ appears between the frequency $\omega_{r,-}$ where $\text{Re}[\xi_-(\omega_{r,-})] = 0$ and the smaller of the two frequencies $\omega_{th,r}$. The width of this plateau increases with decreasing $|b_z|$ since $\omega_{r,-}$ is then pushed to lower frequencies. When this plateau is absent, $\omega_{r,-}$ coincides with the peak in the Kerr angle.

The Kerr angle is zero when η is real (and $1 - |\eta|^2 > 0$) or, equivalently when the wave vectors q_{1+}, q_{2+} are real so that the two electromagnetic waves propagate without attenuation. As we argued above, the effect of b_0 is negligible in the frequency range of Fig. 4 so that we can use Eq. (59) instead of Eq. (58) to compute η . The plateau where $\theta_K = 0$ thus occurs when the two dielectric functions $\xi_{\pm}(\omega)$ are real and positive as can be seen in Fig. 4.

The negative peak at small frequencies in Fig. 4 only occurs when the intraband transitions are included in $\varepsilon(\omega)$ and when b_0 and/or e_F are non-zero so that there is a finite density of electrons and/or holes. We find numerically, for the range of parameters considered, that the position of this peak is at the frequency $\omega_{r,+}$ ($\omega_{r,-}$) where $\text{Re}[\xi_+] = 0$ ($\text{Re}[\xi_-] = 0$) when $b_z < 0$ ($b_z > 0$). Its frequency is redshifted as $|b_z|$ increases. In the opposite case, when $b_{z,r} \rightarrow 0$, we have $\omega_{r,-} - \omega_{r,+} \rightarrow 0$ so that the negative peak merges with the positive peak and the Kerr angle $\theta_K = 0$.

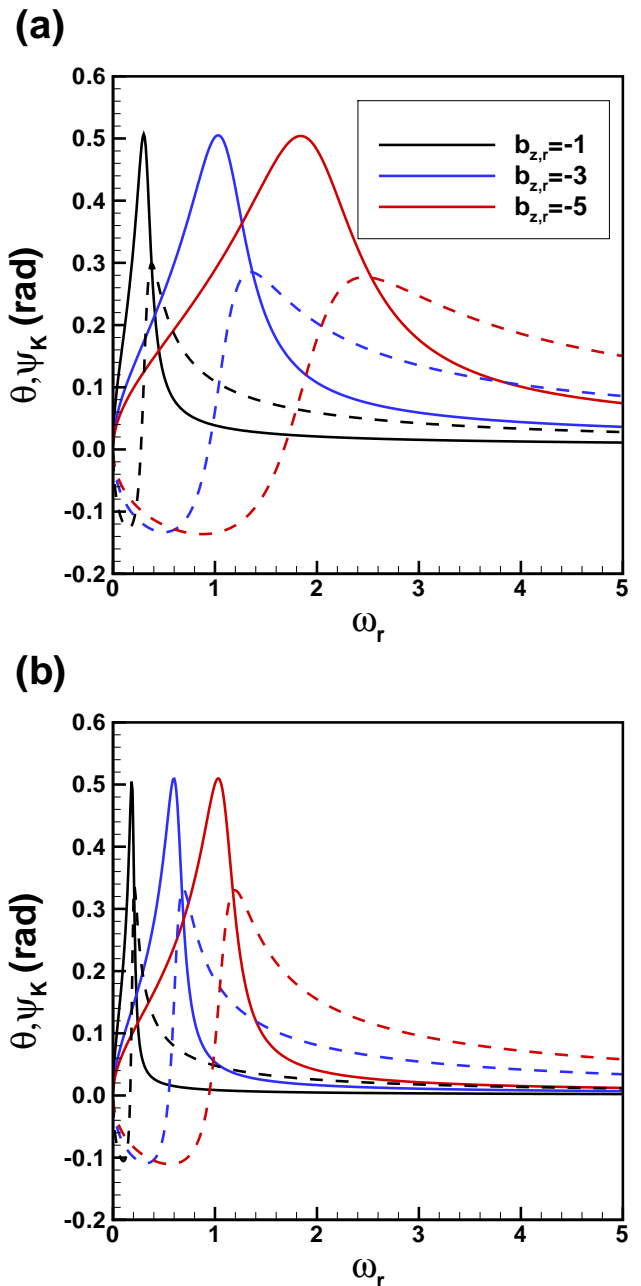


FIG. 3. Frequency behavior of the Kerr (full lines) and ellipticity angles (dashed lines) in the Faraday configuration for a Weyl semimetal in zero magnetic field for several values of the parameters $b_{z,r}$ and with $b_0 = e_F = 0$. The background dielectric function is $\varepsilon_b = 1$ in pannel (a) and $\varepsilon_b = 10$ in pannel (b).

B. Voigt configuration

In the Voigt configuration, the propagation vector and magnetic field are respectively along the x and z axis. Setting $B = 0$ and keeping only b_0 and b_z in the M matrix, the dispersion relations are given by Eq. (68), the polarizations by Eq. (71) and η by Eq. (74) with

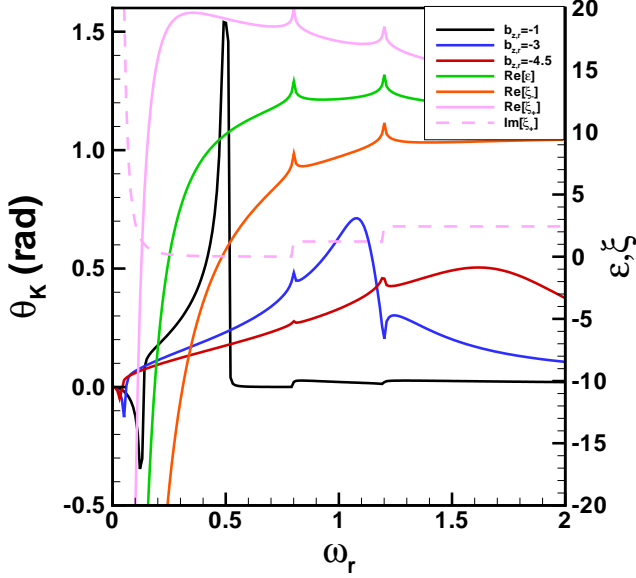


FIG. 4. Kerr angle as a function of frequency in the Faraday configuration for a Weyl semimetal in zero magnetic field and for different values of $b_{z,r}$ and constant $b_{0,r} = 0.1$ and $e_{F,r} = 0.5$. Also shown are the dielectric functions ϵ, ξ_+, ξ_- for $b_{z,r} = -1$.

$\epsilon_{xx} = \epsilon_{yy} = \epsilon_{zz} = \epsilon$. Since the light is incident on a surface with Fermi arcs in this configuration (the Fermi arcs are present on surfaces parallel to the Weyl node separation), their contribution to the conductivity should in principle be taken into account. This contribution was estimated¹³ to be $\sigma_{xy}^s \simeq e^2 \ln(2b_z \lambda) / \pi h$, where λ is the wavelength of light. It is small in comparison with the bulk contribution $\tilde{\sigma}_{xy} = -i\tilde{\epsilon}_{xy}\epsilon_0\omega = e^2 b_z / \pi h$ in the THz range where $\tilde{\epsilon}_{ij}$ is defined in Eq. (37). We thus neglect this contribution in our analysis.

Figure 5 shows the Kerr and ellipticity angles for a finite $b_{z,r}$ at $e_F = b_0 = 0$. Contrary to the case of an ordinary metal, the Kerr rotation angle $\theta_K - \pi/4$ is not negligible in the Voigt configuration. The change of sign of $\theta_K - \pi/4$ occurs numerically at the frequency where $\text{Re}[\epsilon_V(\omega)] = 0$ which is also the frequency at which the ellipticity is maximal. The Kerr angle is positive before the change of sign and is even¹⁴ in b_z . Its maximal value does not change much with b_z but the range of frequencies where the rotation is important increases with $|b_z|$. As in the Faraday case, there is a Kerr effect even in the absence of carriers and even in the Pauli-blocked regime.

Figure 6 shows a more general result where $b_{z,r}, b_{0,r}$ and $e_{F,r}$ are all finite and consequently the Kerr angle has more structure. The two small spikes at frequency above $\omega_r = 0.8$ correspond to the two thresholds for the interband transitions given in Eq. (85). Both transitions are captured in the Kerr angle. The large discontinuities in the Kerr angle correspond to transitions from

$\pi/2$ to $-\pi/2$. These two values give the same angular position for the major axis of the ellipse. There is in consequence no discontinuity in the rotating motion of the polarization ellipse at these frequencies. Between these two peaks, the Kerr angle is almost constant. The separation between the two peaks increases with $|b_{z,r}|$. Note that, with the exception of the very small spikes at the interband threshold, the other two discontinuities occur at $\omega_{r,1}$ and $\omega_{r,2}$ which are defined by $\text{Re}[\epsilon(\omega_{1,r})] = 0$ and $\text{Re}[\epsilon_V(\omega_{2,r})] = 0$. The small negative peak at small frequencies is again due to the intraband transitions and is not present in the absence of carriers. We remark that increasing the relaxation time above $\tau = 10$ ps does not change at all the frequency behavior of the Kerr angle shown in Fig. 6. Reducing τ , however, smooths all discontinuities at low ω_r as shown by the green curve in Fig. 6 for which we took $\tau = 0.1$ ps.

The first peak in the Kerr angle in Fig. 6 occurs at the plasmon frequency as indicated by the red curve. In the limit $\omega\tau \gg 1$ and for $\omega < 2v_F k_{F,\chi}$, Eq. (14) gives $\text{Im}[\epsilon(\omega)] \approx 0$ and

$$\text{Re}[\epsilon(\omega)] \approx \beta(\omega) - \frac{\alpha}{3v_F/c} \frac{4}{\pi\hbar^2} \frac{\hbar^2 b_0^2 + e_F^2}{\omega^2}, \quad (87)$$

where

$$\beta(\omega) = 1 + \frac{\alpha}{6v_F/c} \sum_{\chi} \frac{1}{\pi} \ln \left(\left| \frac{\omega^2 - 4v_F^2 k_c^2}{\omega^2 - 4v_F^2 k_{F,\chi}^2} \right| \right). \quad (88)$$

The plasmon frequency is then given by $\text{Re}[\epsilon(\omega)] = 0$ i.e.,

$$\omega_p = \sqrt{\frac{4\alpha}{3\pi\hbar^2 v_F/c} \frac{\hbar^2 b_0^2 + e_F^2}{\beta(\omega)}}, \quad (89)$$

consistent with the result given in Ref. 34. The intraband plasmon frequency is red-shifted by the interband contribution given by $\beta(\omega)$. Equation (89) can be solved iteratively but a good approximation to the numerical value of the plasmon frequency given in Fig. 6 is obtained by simply taking $\beta(\omega = 0)$ in Eq. (89).

VIII. KERR EFFECT IN A WSM IN A FINITE MAGNETIC FIELD

To study the effect of the magnetic field on the Kerr rotation, we define the dimensionless variables

$$\begin{aligned} v_{F,r} &= \frac{v_F}{c}, b_{z,r} = b_z \ell, \\ b_0 &= b_{0,r} v_F / \ell, e_F = e_{F,r} \hbar v_F / \ell, \\ \omega &= \omega_r v_F / \ell, \end{aligned} \quad (90)$$

and choose $\hbar v_F / \ell = 7.69 v_{F,r} \sqrt{B}$ eV with B in Tesla as our unit of energy. The ratio $v_F / \ell = 1.17 \times 10^{16} v_{F,r} \sqrt{B}$ s⁻¹ so that the frequency $f = \omega / (2\pi) = 1.86 \times$

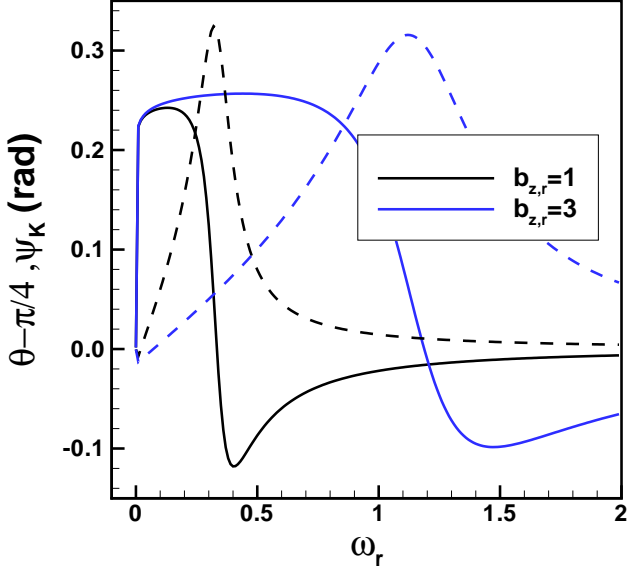


FIG. 5. Frequency behavior of the Kerr rotation angle $\theta_K - \pi/4$ (full lines) and ellipticity angle (dashed lines) ψ_K in the Voigt configuration for a Weyl semimetal in zero magnetic field for two values of $b_{z,r}$ and with $b_0 = e_F = 0$.

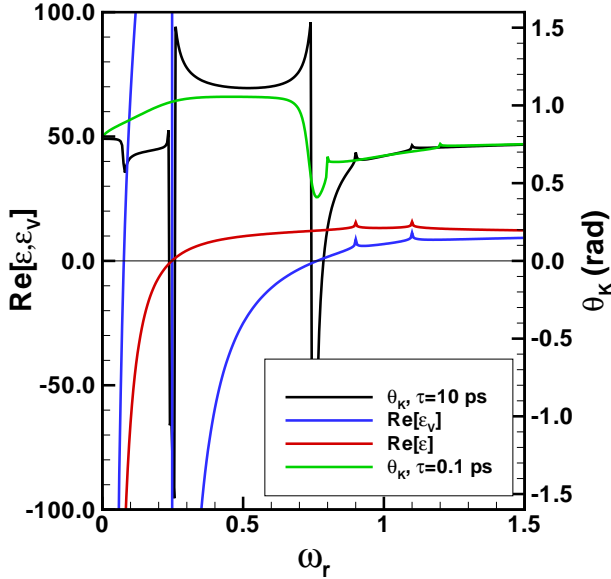


FIG. 6. Frequency behavior of the Kerr angle and real part of the dielectric functions $\varepsilon_V(\omega)$ and $\varepsilon(\omega)$ for a Weyl semimetal in zero magnetic field in the Voigt configuration for the parameters $\varepsilon_{F,r} = 0.5$, $b_{z,r} = 2$, $b_{0,r} = 0.1$ and $\tau = 10$ ps. The green curve gives the Kerr angle for $\tau = 0.1$ ps.

$10^{12}\omega_r\sqrt{B}$ Hz for $v_{F,r} = 0.001$. In terms of these dimensionless parameters, the range of values considered in Sec. VII corresponds to $b_{0,r}, e_{F,r} \in [0, 1.3/\sqrt{B}]$, $b_{z,r} \in [-12.83/\sqrt{B}, 12.83/\sqrt{B}]$ for $v_{F,r} = 0.001$.

We restrict our analysis to the ultraquantum limit where the Fermi level e_F lies in the chiral Landau level of both nodes. The Fermi wave vector in each node, $k_{F,\chi}$, is then given by

$$e_{F,r} = \chi(b_{0,r} - k_{F,\chi,r}\ell) \quad (91)$$

and, in order for the $n \geq 1$ levels to be empty, the condition $e_{F,r} + b_{0,r} < \sqrt{2}$ must be satisfied. The occupation of the Landau levels at $T = 0$ K is given by Eqs. (B1)-(B3) of Appendix B. Since the density of states in one node is $g(E) = 1/4\pi^2\ell^2\hbar v_F$, the Fermi level is given by

$$e_{F,r} = 2\pi^2\ell^3 n_e, \quad (92)$$

where n_e is the total density of charge carriers in the WSM.

To describe the inter-Landau-level transitions, it is more convenient to use negative values of n for the Landau levels in the valence band ($s = -1$). The threshold energy for the absorptive transitions in the $n = -1, 0, 1$ sector are given by

$$\Delta_{0,1}^{(x)} = \sqrt{(e_{F,r} - \chi b_{0,r})^2 + 2} - (e_{F,r} - \chi b_{0,r}), \quad (93)$$

$$\Delta_{-1,0}^{(x)} = \sqrt{(e_{F,r} - \chi b_{0,r})^2 + 2} + (e_{F,r} - \chi b_{0,r}), \quad (94)$$

while for the dipolar transitions (with $n > 0$)

$$\Delta_{-n,n+1}^{(x)} = \sqrt{2|n|} + \sqrt{2(|n| + 1)}, \quad (95)$$

and for the transitions captured by $\sigma_{zz}(\omega)$

$$\Delta_{-n,n}^{(x)} = 2\sqrt{2|n|}. \quad (96)$$

The transitions $\Delta_{0,1}^{(x)}$ ($\Delta_{-1,0}^{(x)}$) appear as peaks in the real part of the conductivity σ_+ (σ_-) where $\sigma_{\pm} = \sigma_{xx} \pm i\sigma_{xy}$, while the dipolar transitions $\Delta_{-n,n+1}^{(x)}$ appear as peaks in both σ_+ and σ_- . The transitions $\Delta_{-n,n}^{(x)}$ appears as peaks in σ_{zz} only. The lowest frequency dipolar transition has the threshold frequency $\omega_r = \Delta_{-1,2}^{(x)} = 3.41$ i.e., $f = 0.32$ THz for $B = 10$ T. As in Sec. VII, we choose $\tau = 10$ ps for the scattering time and limit the summation over Landau levels to $n_{\max} = 10$ unless indicated otherwise. The qualitative aspect of $\theta_K(\omega)$ and $\chi_K(\omega)$ does not change significantly if we increase n_{\max} which is, in any case, limited by the bandwidth of the Weyl cones.

A. Faraday configuration

In the Faraday configuration, the dispersion, polarizations and η are given by Eqs. (53) and (54) and Eqs. (56)

and (58) with ξ_{\pm} defined in Eq. (55). When $b_0 = e_F = 0$, it follows that $\sigma_{xy} = 0$ (since $x_F = 0$ in Eqs. (B6) and (B7)) and so $\varepsilon_{\pm} = \varepsilon_{xx}$. If, in addition, $b_z = 0$, then $\xi_+ = \xi_-$ and $\eta = 0$. As expected the magnetic field alone does not produce a Kerr rotation in the absence of carriers. There is however a Kerr rotation when $b_z \neq 0$ and $e_F = b_0 = 0$ even if there is no carrier in the WSM. There is also a rotation when $e_F = 0$ and $b_0 \neq 0$ i.e., at compensation when the density of electrons is equal to the density of holes. Both carriers contribute the same way to the Kerr angle as pointed out in Sec. VII.

Figure 7 shows a typical result for the Kerr and ellipticity angles as well as for the corresponding dielectric functions ξ_{\pm} . We choose $b_{0,r} = 0.2, b_{z,r} = 0.6, e_{F,r} = 1$. We remark that ξ_- has peaks at the transitions $\Delta_{-1,0}^{(\chi)}$ while ξ_+ captures the transitions $\Delta_{0,1}^{(\chi)}$ for $\chi = \pm$. The dipolar transitions $\Delta_{-n,n+1}^{(\chi)}$ are present in both functions. In Fig. 7, the Kerr angle increases until it reaches a plateau at $\theta_K = \pi/2$ in a small range of frequencies. The onset of the plateau occurs when $\text{Re}[\xi_-(\omega)] = 0$. After the plateau, the Kerr angle drops abruptly to zero and remains zero until the transition at $\omega_r = \Delta_{0,1}^{(-)}$. Discontinuities in $\theta_K(\omega)$ occur at all four transitions in the $n = -1, 0, 1$ sector as well as at all dipolar transitions. The transitions $\Delta_{-n,n}^{(\chi)}$ are not captured by the Kerr angle in the Faraday configuration since ε_{zz} does not enter its calculation. Other transitions will appear in $\theta_K(\omega)$ if the Weyl cones are tilted since a tilt modifies the matrix elements of the current operator and so the selection rules^{15,22}.

It may seem that there is a discontinuous change in the Kerr angle from $\pi/2$ to 0 at $\omega_r = 0.34$ in Fig. 7. This is however not the case since both the rotation and the ellipticity of the Kerr polarization change with frequency. We illustrate this in Fig. 8 where we plot the trajectory of the electric polarization vector for one cycle of oscillation at different frequency points and for the parameters used in Fig. 7. The trajectory is an ellipse with its major axis at $\theta_K = \pi/2$ at point 3 and becomes a quasi circle at points 4 and 5. This circle is then elongated along E_x at points 6 and 7 and the major axis is now at $\theta_K = 0$. There has been, however, no discontinuous change in the trajectory of the electric polarization vector in between these points.

With $b_z = 0$ and a finite Fermi level $e_{F,r} = 1$, the magnetic field leads to a positive Kerr angle as shown by the black line in Fig. 9. With our sign convention for b_z and b_0 , a positive value of $b_{z,r}$ leads to a negative Kerr angle in the absence of a magnetic field, as shown in Sec. VII. Thus, at small frequencies increasing $b_{z,r}$ progressively reduces the region where the Kerr angle induced by the magnetic field is large. (In the opposite case where $b_{z,r} < 0$, increasing $|b_{z,r}|$ increases the region where the Kerr angle is large). Further increasing $b_{z,r}$ changes the sign of the Kerr angle and decreases it to zero. The plateaus where the Kerr angle is precisely zero or $\pi/2$ are in a frequency range where ξ_{\pm} are both real

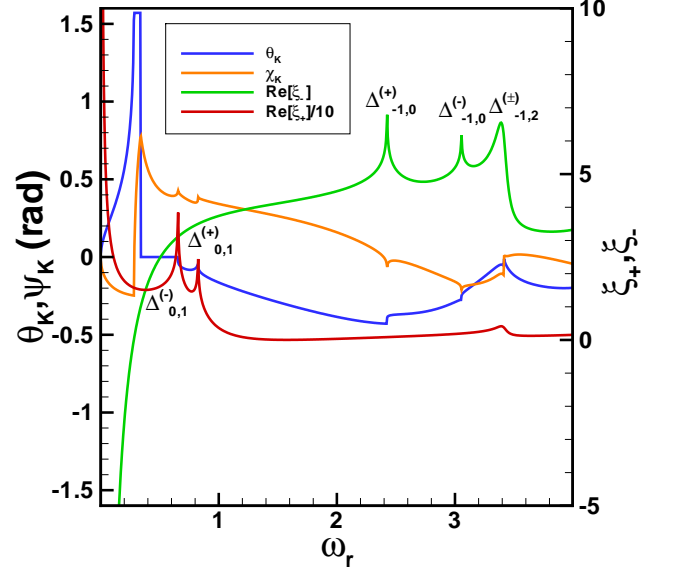


FIG. 7. Frequency behavior of the Kerr and ellipticity angles and real part of the dielectric functions ξ_-, ξ_{+-} for a Weyl semimetal in a magnetic field and in the Faraday configuration. Parameters $e_{F,r} = 1, b_{0,r} = 0.2$ and $b_{z,r} = 0.6$. The $\Delta_{n,m}^{(\pm)}$ symbols indicate the inter-Landau-level transitions.

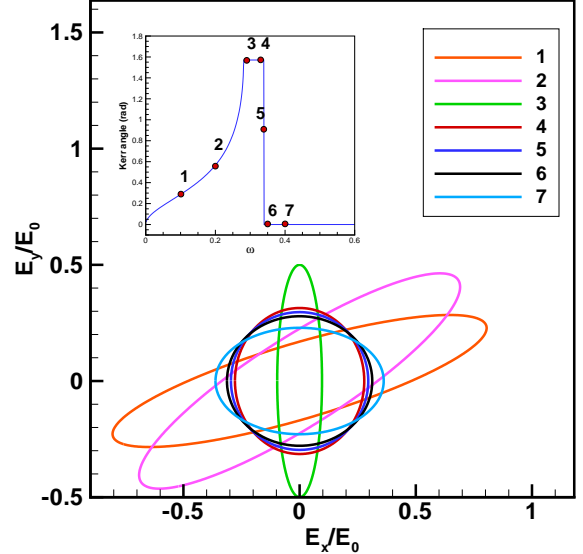


FIG. 8. Trajectories of the polarization vector for the different frequency points identified in the inset. The sharp drop in the Kerr angle corresponds to a continuous change in the shape of the ellipse. The parameters are those of Fig. 7.

and positive so that η is imaginary and $\tan(2\theta_K) = 0$ or π depending on the sign of $1 - |\eta|^2 < 0$ in Eq. (60). These two plateaus disappear when $b_{z,r} \leq 0$.

An interesting result of our calculation is that at precisely $b_{z,r} = e_{F,r}$, with $g = 0$ in the matrix M , the Kerr angle is zero in the range $\omega_r \in [0, \Delta_{0,1}^{(-)}]$ i.e., up to the smallest of the four transition frequencies in the $n = -1, 0, 1$ sector. In this region, we find numerically that $\text{Re}[\eta] = 0$ and $1 - |\eta|^2 > 0$ in Eq. (60) so that $\theta_K = 0$. We do not observe this behavior when $B = 0$. Indeed, this result is due to the particular form of the conductivity tensor in the extreme quantum limit i.e., to the fact that $\text{Re}[\sigma_{xx}] = \text{Im}[\sigma_{xy}] = 0$ for $\omega_r < e_{F,r}$. If we expand the conductivity σ_{xx} and σ_{xy} to first order in ω_r , we find that

$$\xi_{\pm} = 1 - \frac{2 \text{Im}[\sigma_{xx}]}{\omega \varepsilon_0} > 0, \quad (97)$$

so that $q_{1,+}, q_{2,+}$ in Eqs. (53) and (54) are real and positive and $\text{Re}[\eta] = 0$. The axion term b_z in ξ_{\pm} cancels the gyrotropic contribution from the ε_{xy} in this limit. Equation (97) is satisfied not just at small frequencies but for $\omega_r \in [0, \Delta_{0,1}^{(-)}]$, something we were only able to check numerically. This observation can provide a way to measure the axion term b_z if the Fermi level is known. When $g = 1$ (or $g = 1/3$), the Kerr angle is zero but only in the range $\omega_r \in [\omega_{a,r}, \Delta_{0,1}^{(-)}]$ where $\omega_{a,r} \approx 0.0001$ i.e., a very small frequency. Below $\omega_{a,r}$ we find that $1 - |\eta|^2 < 0$ and the Kerr angle is $\theta_K = \pi/2$. This remains true if $b_z = e_F = 0$ so that it would seem that the axion term b_0 causes a rotation of the polarization from \hat{x} to \hat{y} at very small frequency if g is not zero, another curious (or spurious) effect of a finite b_0 at $\omega \rightarrow 0$.

Another interesting fact when $\omega_r \in [0, \Delta_{0,1}^{(-)}]$ and $b_{z,r} = e_{F,r}, g = 0$ is that the wave vectors $q_{1,\pm}$ and $q_{2,\pm}$ are real and positive and their dispersions are linear in q and gapless so that the two modes propagate without attenuation as shown in Fig. 9(b). However, as soon as $b_{z,r} \neq e_{F,r}$, only one of the two modes remains gapless with a $\omega \sim q^2$ dispersion (if $b_0 = 0$). In the low-magnetic field limit where the semi-classical Boltzmann equation is used to compute the conductivity tensor, this mode would be the helicon mode discussed in Ref. 35.

When b_0 is finite Eqs. (53) and (54) give that the mode $q_{2,+}$, that propagates in the positive z direction and $q_{1,-}$, a mode propagating in the opposite direction have a finite wave vector $q\ell = \frac{\kappa b_0 \ell}{c} = \kappa v_{F,r} \approx 10^{-5}$ at $\omega = 0$. This sort of instability in chiral matter and some of its consequences have been discussed before³⁶. In this reference however, b_0 is associated with the chiral magnetic effect (CME) i.e., with a difference in the chiral potential of the two nodes. In our case, the Fermi pockets are in chemical equilibrium with a common Fermi level and b_0 is related to the difference in energy between the two Dirac points, a property of the band structure of the WSM. There is a

gyrotropic current in this case²³ but it should vanish in the static limit. In fact, according to Ref. 24, the gyromagnetic contribution of b_0 and its associate current in the Maxwell equations should be suppressed by scattering at low frequency. If this is the case, this instability would vanish. In any case, our results in the THz range are not affected by the presence of this possible gap in the wave vector at very low frequency.

B. Voigt configuration

We consider an incident wave propagating along the x axis with the external magnetic field again in the z direction. The dispersion relations are given by Eq. (68), the polarizations by Eq. (71) and η by Eq. (74). As for the $B = 0$ case, the same numerical results are obtained by using the simpler formulas with $g = 0$ (b_0 must be kept in the dielectric tensor, however).

Figure 10 shows $\theta_K(\omega)$ for the same parameters as those used in Fig. 9 for the Faraday configuration. Since ε_{zz} now enters in the calculation of the Kerr angle and because the intra-Landau level transitions in $n = 0$ are included in ε_{zz} , we must also specify the magnetic field and the relaxation time in addition to the dimensionless variables $b_{0,r}, b_{z,r}, e_{F,r}$ and ω_r . The Kerr angle has a plateau at $\theta_K = \pi/4$ (i.e., no effective rotation of the polarization) at small frequencies before dropping abruptly to $\theta_K = -\pi/4$. As in the Faraday case, small spikes signal the dipolar transitions $\Delta_{-1,2}^{(x)} = 3.42$, $\Delta_{0,1}^{(x)} = 0.73$ and $\Delta_{-1,0}^{(x)} = 2.73$. A unique feature of the Voigt configuration is that the transitions $\Delta_{-n,n}^{(x)}$ are now present in $\theta_K(\omega)$. Increasing $b_{z,r}$ decreases the width of the plateau where $\theta_K = \pi/4$ and so increases the range of frequencies where the effective rotation angle is important. Contrary to what we found in the Faraday configuration, θ_K is not zero when $b_{z,r} = e_{F,r}$ but its frequency profile is distinctively different, at low frequency, than the profiles for $b_{z,r} \neq e_{F,r}$.

Another feature of the Voigt configuration is that θ_K has a change of curvature and a zero ellipticity at a frequency where $\varepsilon_{zz}(\omega) = 0$ i.e., at the plasmon frequency ω_p as indicated in Fig. 11. This feature is also present in Fig. 10 but difficult to see because of the superposition of the different curves. If we consider only the intra-band transitions, we have from $\varepsilon_{zz}(\omega) = 0$ in the limit $\omega\tau \gg 1$ that the plasmon frequency is given by

$$\omega_p = \sqrt{\frac{e^3 v_F B}{2\pi^2 \hbar^2 \varepsilon_0}}, \quad (98)$$

which is the known result⁷ for two nodes. The plasmon frequency is independent of the relaxation time in this limit. The $\omega_p \sim \sqrt{B}$ behavior is an experimental signature of a WSM²⁶ and of the chiral anomaly. This frequency is corrected by inter-Landau-level transitions and

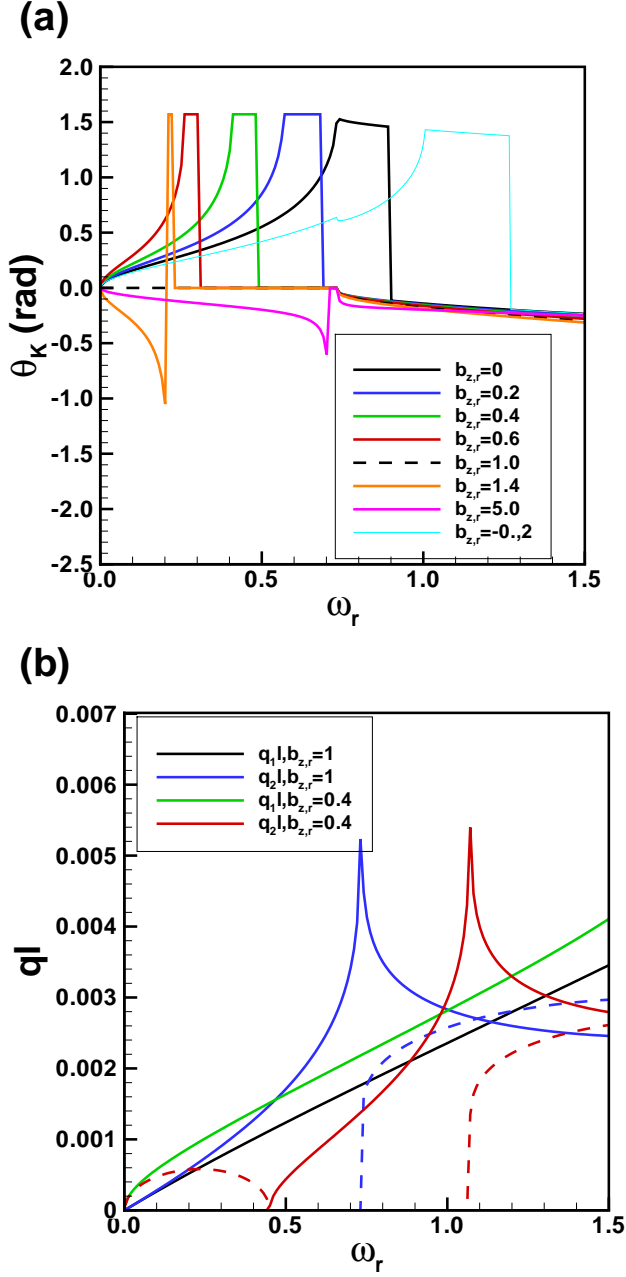


FIG. 9. (a) Kerr angle as a function of frequency for a Weyl semimetal in a magnetic field and in the Faraday configuration for different values of $b_{z,r}$ and with $e_{F,r} = 1, b_{0,r} = 0$ and $n_{mzx} = 20$. (b) Real (full lines) and imaginary part (dashed lines) of the wave vector ql for $e_{F,r} = 1, b_{0,r} = 0$ and $b_{z,r} = 0.4, 1.0$.

scattering. The more accurate result is found by solving the self-consistent equation

$$\omega_p = \sqrt{\frac{2e^3 v_F B}{4\pi^2 \epsilon_0 \hbar^2} \frac{1}{1 - \frac{8\alpha c \Lambda(\omega_{p,r})}{\pi v_F}} - \frac{1}{\tau^2}}, \quad (99)$$

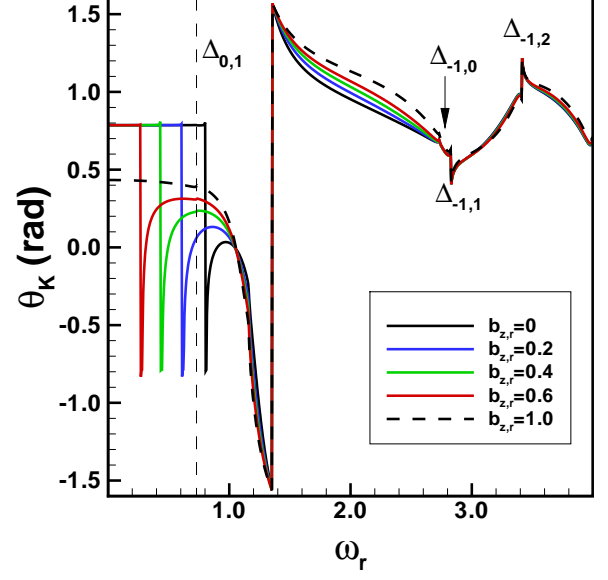


FIG. 10. Kerr angle as a function of frequency for a Weyl semimetal in a magnetic field and in the Voigt configuration for different values of $b_{z,r}$ and with $e_{F,r} = 1, b_{0,r} = 0, B = 10$ T, $\tau = 10$ ps. The rotation angle is $\theta_K - \pi/4$. The Landau level transitions indicated by the $\Delta_{n,m}$ symbols have the same value for both nodes since $b_0 = 0$.

where

$$\Lambda(\omega_r) = \sum_{n>0} n \int_0^{+\infty} dx \frac{1}{(x^2 + 2n)^{3/2}} \frac{1}{\omega_r^2 - 4(x^2 + 2n)}. \quad (100)$$

A very good approximation of the plasmon frequency found in Fig. 11 is obtained by taking $\omega_r = 0$ in $\Lambda(\omega_r)$. The inter-Landau-level transitions decrease the plasmon frequency because $\Lambda < 0$ when $\omega_r < \sqrt{2}$. Figure 11 also shows that the end of the plateau where $\theta_K = \pi/4$ and the negative peak leading to $\theta_K = -\pi/4$ are at a frequency corresponding to $\text{Re}[\varepsilon_V(\omega)] = 0$ as in the $B = 0$. The negative peak, however, does not disappear if $e_F = b_0 = 0$ and is not due to the intraband transitions.

IX. EFFECT OF \mathbf{b}_\perp ON THE KERR ANGLE

We study in this section the effect of a perpendicular component \mathbf{b}_\perp on the Kerr angle. To obtain analytical results that are manageable, we set $g = 0$ in the matrix M but keep b_0 in the conductivity tensor. The magnetic field is again along the z axis and the light propagates along that axis. The M matrix is

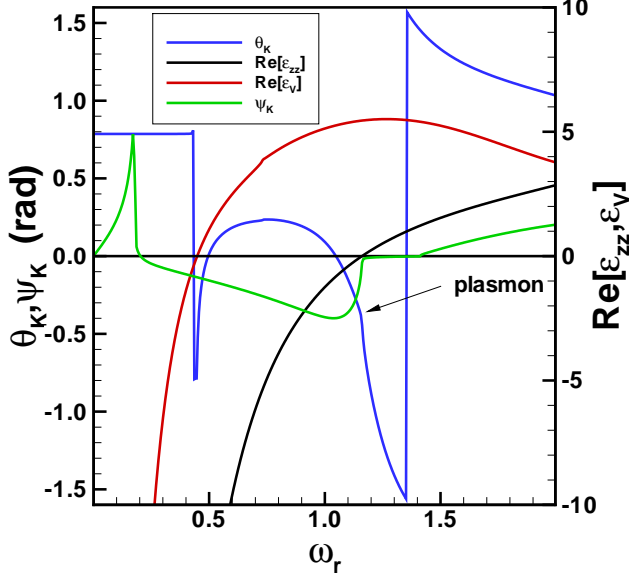


FIG. 11. Frequency behavior of the Kerr and ellipticity angles and of the real part of the dielectric functions ε_{zz} and ε_V for a Weyl semimetal in a magnetic field and in the Voigt configuration. The actual rotation of the polarization is $\theta_K - \pi/4$. Parameters: $b_{z,r} = 0.2$, $e_{F,r} = b_{0,r} = 0$, $B = 10$ T and $\tau = 10$ ps. The kink in the Kerr angle is at the plasmon frequency.

$$M = \begin{pmatrix} \omega^2 \varepsilon_{xx} - c^2 q_z^2 & \omega^2 \varepsilon_{xy} + i\omega c \kappa b_z & -i\omega c \kappa b_y \\ -\omega^2 \varepsilon_{xy} - i\omega c \kappa b_z & \omega^2 \varepsilon_{xx} - c^2 q_z^2 & i\omega c \kappa b_x \\ i\omega c \kappa b_y & -i\omega c \kappa b_x & \omega^2 \varepsilon_{zz} \end{pmatrix}. \quad (101)$$

With the axion term in spherical coordinates

$$\mathbf{b} = b \sin \theta \cos \varphi \hat{\mathbf{x}} + b \sin \theta \sin \varphi \hat{\mathbf{y}} + b \cos \theta \hat{\mathbf{z}}, \quad (102)$$

the dispersion relations and corresponding polarizations are given by

$$q_{\pm}^2 = -\frac{\kappa^2}{2\varepsilon_{zz}} \Lambda_{\pm}(\theta, \varphi = 0, b), \quad (103)$$

where

$$\Lambda_{\pm}(\theta, \varphi, b) = b^2 \sin^2 \theta \cos(2\varphi) \pm \sqrt{b^4 \sin^4 \theta + \frac{4\omega^2 \varepsilon_{zz}^2}{c^2 \kappa^2} \left(b \cos \theta - i \frac{\omega \varepsilon_{xy}}{c \kappa}\right)^2} \quad (104)$$

and (for $b \neq 0$)

$$\mathbf{e}_{\pm} = \frac{1}{\sqrt{|E_{x,\pm}|^2 + |E_{z,\pm}|^2 + 1}} \begin{pmatrix} E_{x,\pm} \\ 1 \\ E_{z,\pm} \end{pmatrix}, \quad (105)$$

where we have defined

$$E_{x,\pm} = \frac{2i \frac{\omega \varepsilon_{zz}}{c \kappa} \left(b \cos \theta - i \frac{\omega \varepsilon_{xy}}{c \kappa}\right) + b^2 \sin^2 \theta \sin 2\varphi}{\Lambda_{\pm}(\theta, \varphi, b)}, \quad (106)$$

and (for $\varepsilon_{zz} \neq 0$)

$$E_{z,\pm} = -ib \sin \theta \frac{E_{x,\pm} \sin \varphi - \cos \varphi}{\frac{\omega \varepsilon_{zz}}{c \kappa}}. \quad (107)$$

There is a component of the polarization in the direction of propagation of the wave when $\theta \neq 0$.

If the polarization of the incident wave is along the x axis, the function η that enters in the calculation of the Kerr angle is given by (with $E_y = 1$)

$$\eta = \frac{-2 \left(\frac{q_+}{q_0} - \frac{q_-}{q_0}\right)}{\left(1 - \frac{q_+}{q_0}\right) \left(1 + \frac{q_-}{q_0}\right) E_{x,+} - \left(1 + \frac{q_+}{q_0}\right) \left(1 - \frac{q_-}{q_0}\right) E_{x,-}}, \quad (108)$$

where $q_0 = \omega/c$. Since, the rotational symmetry in the $x - y$ plane is broken, the Kerr angle changes with the azimuthal angle φ and depends on the orientation of the polarization vector of the incident wave.

Figure 12 shows the Kerr angle for several orientations of the axion term \mathbf{b} for $e_{F,r} = 1$, $|\mathbf{b}_r| = 0.4$ and $b_{0,r} = 0$. The frequency domain where θ_K is large increases with the polar angle θ if e_F is not zero. This is consistent with the behavior shown in Fig. 9 since a finite $\theta \in [0, \pi/2]$ decreases $b_{z,r}$ when $|\mathbf{b}_r|$ is fixed. When $\varphi = 0, \pi/2$ and $\theta \neq 0$, a new peak appears on the right of the plateau where $\theta_K = \pi/2$ and increases in amplitude with $\theta \in [0^+, \pi/2]$. The frequency at which $\theta_K = 0$ on the left side of this peak is the plasmon frequency. Indeed, when, $\text{Re}[\varepsilon_{zz}] = 0$, $\text{Im}[\varepsilon_{zz}] \approx 0$, $\theta = \pi/2$ and $\varphi = 0, \pi/2$, Eq. (106) becomes $E_{x,\pm} = 0$ so that $\eta \rightarrow \infty$ and $\theta_K = 0$.

We found previously that a nonzero b_z gives a Kerr angle even in the absence of carriers. In the present case, if $\theta = \pi/2$, $\varphi = 0$ and $e_F = b_0 = 0$ (no carriers), the Kerr angle is zero at all frequencies (not shown in Fig. 12).

Figure 9 shows that when $b_{z,r} = e_{F,r}$ and $g = 0$, the Kerr angle is zero in the frequency range $\omega_r \in [0, \Delta_{0,1}^{(-)}]$. This remains true if \mathbf{b} is tilted with b_z kept constant at $b_{z,r} = e_{F,r}$ and $\varphi = 0$.

X. MAGNETIC FIELD BEHAVIOR OF THE KERR ANGLE

We end our study of the Kerr rotation in a WSM by considering the situation where the frequency f is kept fixed and the magnetic field is varied. We restrict our analysis to the Faraday configuration. Figure 13 shows the Kerr angle for $f = 5$ THz, $b = 5 \times 10^8 \text{ m}^{-1}$, $\varphi = 0$, $v_F = 3 \times 10^5 \text{ m/s}$, $n_e = 10^{21} \text{ m}^{-3}$, $\tau = 10$ ps and $b_0 = 0$. Note that the dimensionless parameters $b_r, b_{0,r}, \omega_r, e_{F,r}$ that enter the calculation of the conductivity tensor and the M matrix change with magnetic field. In addition the Fermi level e_F decreases with increasing B when the density is fixed. To observe any transition in $\theta_K(B)$, we must ensure that f is chosen such that $\omega_r = 2\pi f/(v_F/\ell)$ goes through the different inter-Landau-level transitions when the magnetic field is varied. In addition, in order

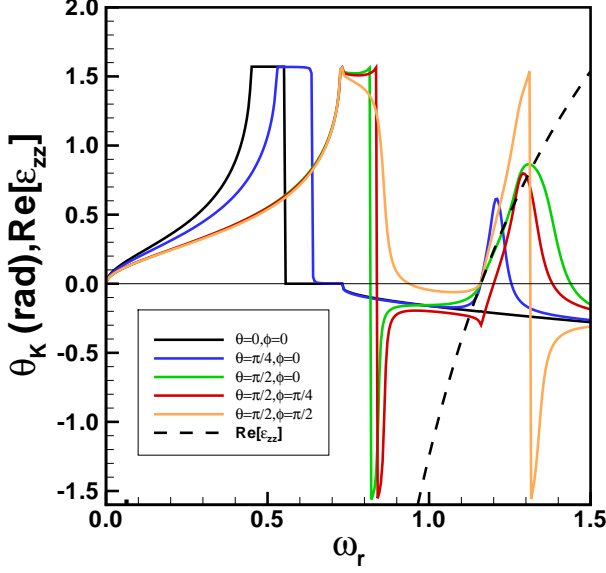


FIG. 12. Kerr angle as a function of frequency for a Weyl semimetal in a magnetic field and in the Faraday configuration for different orientations of the vector \mathbf{b} and with $e_{F,r} = 1, b_{0,r} = 0, b = 0.4$ and real part of the dielectric function ε_{zz} near $\varepsilon_{zz} = 0$.

to capture the plasmon mode, ω_r must intersect the frequency $\omega_{p,r}$ where $\varepsilon_{zz}(\omega_{p,r}) = 0$ and θ must be finite. Finally, the condition $e_{F,r} + b_{0,r} < \sqrt{2}$ must be satisfied at all B in order for the WSM to stay in the ultra-quantum limit where our analysis is valid. The magnetic field range $B \in [0.5, 6]$ T with the above parameters satisfy these conditions.

The black curve in Fig. 13 is the function $\theta_K(B)$ for the special case where $b = 0$ thus showing the effect of the magnetic field alone. We see that $\theta_K(B) = 0$ when the magnetic field is such that $\omega_r < \Delta_{-1,0}$ which is the lowest-energy transition when the Fermi level is above the Dirac point. At lower B , the transitions $\Delta_{-1,2}$ and $\Delta_{0,1}$ are captured by the Kerr angle. The transition $\Delta_{-1,1}$ is captured only if $\theta \neq 0$ because it is only then that $\varepsilon_{zz}(\omega)$, which contains these transitions, enters in the equation for the Kerr angle.

When θ is non-zero, a downward turn appears in $\theta_K(B)$ above the magnetic field B^* for which $\varepsilon_{zz}(\omega_{p,r}) = 0$ (note that, in our reduced units, $\omega_{p,r}$ is independent of B in the clean limit). For $B > B^*$, Fig. 13 shows that $|\theta_K(B)|$ increases with θ and the shoulder is pushed to higher B . The Kerr angle is effectively zero from B^* to the shoulder and tends to a constant at large B .

The Fermi level $e_{F,r} \sim 1/B^{3/2}$ and frequency $\omega_r \sim$

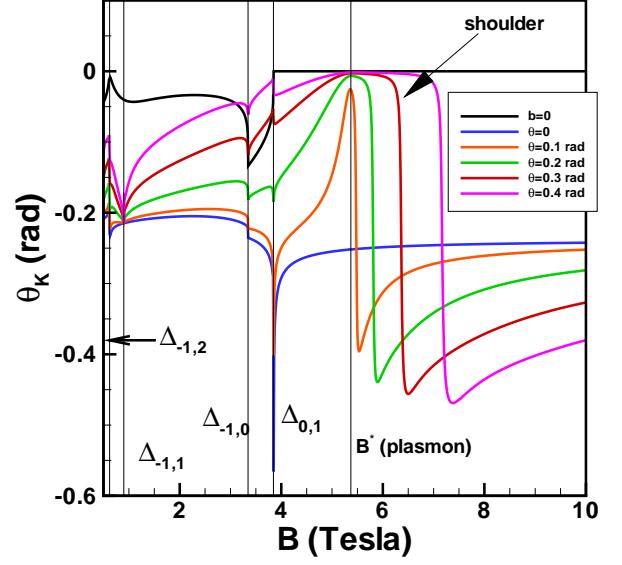


FIG. 13. Behavior of the Kerr angle with magnetic field at fixed frequency $f = 5$ THz in the Faraday configuration for different inclination angles θ of the axion term \mathbf{b} . The parameters are $b = 5 \times 10^8 \text{ m}^{-1}$, $n_e = 10^{21} \text{ m}^{-3}$, $\tau = 10 \text{ ps}$, $v_F = 3 \times 10^5 \text{ m/s}$, $\varphi = 0$ and $b_0 = 0$. The black curve is for $b = 0$.

$1/B^{1/2}$ so that, in the limit of very large B , $\varepsilon_{xy} \rightarrow 0$ and

$$\begin{aligned} \varepsilon_{xx}^* &\equiv \varepsilon_{xx}(B \rightarrow \infty) \\ &= 1 + \frac{\kappa}{2v_{F,r}} \left(1 + 2 \sum_{n>1} \int_{-\infty}^{+\infty} dx \frac{\Lambda_n(x)}{\Delta_n^3(x)} \right), \end{aligned} \quad (109)$$

where $\Lambda_n(x)$ and $\Delta_n(x)$ are defined in Appendix B. The constant ε_{xx}^* is real and positive. We thus have, from Eqs. (55) and (59,) that

$$\xi_{\pm} = \varepsilon_{xx}^* \mp \frac{c\kappa b_z}{\omega} \quad (110)$$

and the function η that enters the formula for the Kerr angle is, for $\theta = 0$ and $b_0 = 0$, given by

$$\eta = \frac{i \left(\sqrt{\varepsilon_{xx}^* + \frac{c\kappa b_z}{\omega}} - \sqrt{\varepsilon_{xx}^* - \frac{c\kappa b_z}{\omega}} \right)}{1 - \sqrt{\varepsilon_{xx}^* - \left(\frac{c\kappa b_z}{\omega} \right)^2}}. \quad (111)$$

The Kerr angle in this limit is plotted in Fig. 14 as a function of b_z for $f = 5$ THz and $B = 20$ T. On the positive axis, the Kerr angle is zero at small b_z where $1 - |\eta|^2 > 0$ and changes abruptly to $\theta_K = -\pi/2$ when $1 - |\eta|^2 < 0$ [see Eq. (60)]. As b_z increases further, $|\theta_K|$ decreases. The end of the plateau where $\theta = -\pi/2$ is at $b_z^* = \omega \varepsilon_{xx}^* / c\kappa$. Note that, since $\varepsilon_{xy} \rightarrow 0$, the magnetic field has no effective rotating power at large B . Figure 14 shows that the Kerr angle is odd in b_z as expected in the Faraday configuration.

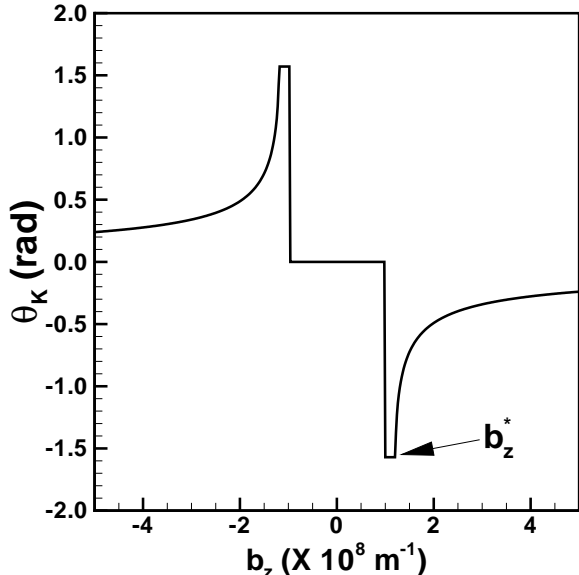


FIG. 14. Kerr angle as a function of the axion term b_z in the limit of large magnetic field and for $B = 20$ T, $f = 5$ THz, $\theta = \varphi = 0$, $n_e = 10^{21} \text{ m}^{-3}$, $v_F = 3 \times 10^5$ m/s, $b_0 = 0$.

XI. CONCLUSION

We have studied the effect of the axion terms b_0 and \mathbf{b} on the magnetic field and frequency profile of the Kerr angle using a simple two-node model of a Weyl semimetal with broken time reversal and/or inversion symmetries. We have considered the effect of the axion terms alone and then in the presence of an external static magnetic field. In both cases, our study was made in the Faraday and Voigt configurations. When a magnetic field was considered, we analyzed the Kerr rotation in the ultra-quantum regime where the Fermi level lies in the chiral Landau level. For the case $\mathbf{B} = 0$, our study complements earlier works on the subject while the $\mathbf{B} \neq 0$ case, with the axion terms, has not been studied before.

The Kerr angle has a rich frequency behavior which depends sensitively on the value of the different parameters of the WSM. We find that it can be quite large, reaching its maximum value $\theta_K = \pm\pi/2$ at certain frequencies. The gyrotropic power of \mathbf{b} is much bigger than that of b_0 which, in our calculations, has mainly the effect of unbalancing the electronic density in both nodes. Depending on its orientation with respect to the external magnetic field, the axion term \mathbf{b} can increase or decrease the Kerr rotation caused by the magnetic field. Moreover, the axion term \mathbf{b} , contrary to the magnetic field \mathbf{B} , enforces a Kerr rotation even when the Fermi level $e_F = 0$ (i.e., no electronic density in both nodes if $b_0 = 0$ or equal density of electrons and holes if $b_0 \neq 0$).

Allowed electronic transitions are captured by the frequency or magnetic field profile of the Kerr angle. The

Faraday and Voigt configurations capture a different set of transitions. In the Voigt configuration and with $\mathbf{B} \neq 0$, the frequency of the plasmon mode is signaled by a small kink in $\theta_K(\omega)$. The plasmon mode also appears in $\theta_K(\mathbf{B})$ if the vector \mathbf{b} is slightly tilted with respect to the external magnetic field.

In the ultra-quantum limit, the particular form of the dielectric function of the Weyl semimetal allows the Kerr angle to be zero in a large range of frequencies in the Faraday configuration. More interestingly, this range can extend all the way down to $\omega = 0$ in the particular case where the component of the axion term along the magnetic field satisfies the condition $b\hbar v_F = e_F$ (for $\mathbf{b} \parallel \mathbf{B}$) and the axion term b_0 is absent from the Maxwell equations.

There are very few measurements of the Kerr angle in WSMs reported in the literature. Most of them measure the Faraday rotation. In Ref. 37, however, a large Kerr rotation of $\theta_K = 0.056$ rad was measured in the magnetic WSM $\text{Co}_3\text{Sn}_2\text{S}_2$, which hosts three pairs of Weyl nodes³⁸, in a weak magnetic field at a photon energy of $\hbar\omega = 0.1$ eV (in the infrared spectrum). This angle is large in comparison with that measured in ferromagnetic metals.

In this paper, we used the simplest hamiltonian possible for a time-reversal symmetry broken WSM in order to isolate the effect of the axion terms b_0 and/or b_z on the Kerr rotation. To our knowledge, there is a present no known WSM with this idealized electronic dispersion and a single pair of Weyl nodes. Most WSMs have several pairs or nodes with a certain amount of tilt, anisotropy, and nonlinearity in the dispersion. From a previous study by one of us¹⁵ where the axion terms were not considered, we know that the Kerr rotation, in a magnetic field, is also dependent on the tilt of each node. It is, of course, possible to extend the approach used in our paper to a WSM with an arbitrary number of pairs of nodes (possibly tilted) by calculating the total conductivity tensor if the parameters of each node as well as their position in energy with respect to the common Fermi level are known. It would be difficult, then to isolate the contribution of the axion terms to the Kerr rotation.

Magnetic Weyl semimetals with a single pair of Weyl nodes are hard to find but recent *ab initio* calculations^{39,40} and ARPES⁴⁰ measurements have shown that EuCd_2As_2 in a magnetic field greater than $B_c = 1.6$ T applied along its c axis is a Weyl semimetal with a single pair of tilted Weyl nodes. In this WSM, $b_0 = 0$ and $b_z = 2.6 \times 10^8 \text{ m}^{-1}$ and b_z is found to be almost constant for $B > B_c$. The magnetic Weyl semimetal $\text{K}_2\text{Mn}_3(\text{AsO}_4)_3$ is also predicted by first-principles calculations to host a single pair of nodes⁴¹. In both cases, however, the low-energy hamiltonian is more complex than the one used in our paper. Moreover, Kerr rotation measurements on these model Weyl semimetals have not yet been done.

ACKNOWLEDGMENTS

R. C. was supported by a grant from the Natural Sciences and Engineering Research Council of Canada (NSERC).

Appendix A: CONDUCTIVITY TENSOR OF THE WSM FOR $\mathbf{B} = 0$

The conductivity of a Weyl node is the sum of the interband and intraband contributions. The interband term is obtained by calculating the current-current response function in the clean limit as given by Eq. (11). At $T = 0$ K, using the results of Sec. II, we find

$$\sigma_{\chi,inter}(\omega) = \frac{e^2\omega}{12\hbar v_F} [\theta(\omega - 2v_F |k_{F,\chi}|) \quad (\text{A1}) \\ - \frac{i}{\pi} \ln \left(\left| \frac{\omega^2 - 4v_F^2 k_c^2}{\omega^2 - 4v_F^2 k_{F,\chi}^2} \right| \right)],$$

where $v_F k_c$ is a ultraviolet cutoff and $k_{F,\chi}$ is the Fermi wave vector in each node which is related to b_0 and the Fermi level e_F by Eq. (13).

For the intraband conductivity, it is necessary to include disorder and the retarded current-current response is then given by

$$\chi_{\chi}^{(xx)}(\omega) = \frac{e^2 v_F^2}{V \hbar} \sum_s \sum_{\mathbf{k}} \left| \eta_{\chi,s}^{\dagger}(\mathbf{k}) \sigma^{(x)} \eta_{\chi,s'}(\mathbf{k}) \right|^2 \quad (\text{A2}) \\ \times \int_{-\infty}^{+\infty} d\omega' \int_{-\infty}^{+\infty} d\omega'' A_{\chi,s}(\mathbf{k}, \omega') A_{\chi,s}(\mathbf{k}, \omega'') \\ \times \frac{F(\omega'') - F(\omega')}{\omega + i\delta + \omega'' - \omega'},$$

where $F(\omega) = 1/(e^{\beta\hbar\omega} + 1)$ with $\beta = 1/k_B T$ and $A_{\chi,s}(\mathbf{k}, \omega)$ is the spectral weight of the disorder averaged Green's function $\langle G_{\chi,s}^R(\mathbf{k}, \omega) \rangle$ which is given by

$$\langle G_{\chi,s}^R(\mathbf{k}, \omega) \rangle = \int_{-\infty}^{+\infty} d\omega' \frac{A_{\chi,s}(\mathbf{k}, \omega')}{\omega + i\delta - \omega'}. \quad (\text{A3})$$

We take for the spectral weight the Lorentzian form

$$A_{\chi,s}(\mathbf{k}, \omega) = \frac{\Gamma/\pi}{(\omega - (E_{\chi,s}(\mathbf{k}) - \hbar v_F k_{F,\chi})/\hbar)^2 + \Gamma^2}, \quad (\text{A4})$$

where $\Gamma = 1/2\tau$ and τ is the scattering time. After a lengthy calculation, we recover the result (the real part of this conductivity is derived in Ref. 19).

$$\sigma_{\chi,intra}(\omega) = \frac{e^2}{6\pi^2 \hbar^3 v_F} \frac{\tau}{1 + \omega^2 \tau^2} \left[e_{F,\chi}^2 + \frac{1}{3} \hbar^2 \omega^2 \quad (\text{A5}) \right. \\ \left. + \frac{\hbar^2}{4\tau^2} + i\omega\tau (e_{F,\chi}^2 - e_C^2) \right],$$

where e_C is an energy cutoff in the valence band. The constant e_C^2 can be fixed by requiring that $\sigma_{\chi}(\omega)$ satisfies the Kramers-Kronig relations. We find in this way that $e_C^2 = \hbar^2/12\tau^2$.

Appendix B: CONDUCTIVITY TENSOR OF THE WSM FOR $\mathbf{B} \neq 0$

Formulas for the absorptive parts of the dynamic conductivity tensor due to interband transitions in a simple two-node model with $b_0 = 0$ are given in Ref. 42. In this Appendix, we extend these results to compute the complete dynamic conductivity tensor in the ultra quantum limit, allowing for different populations for the two nodes. We use the dimensionless variables defined in Eq. (90) and the current-current response tensor defined in Eq. (30). In the ultra-quantum limit where the Fermi level is in the chiral level i.e., we must respect the condition $|e_{F,\chi,r}| < \sqrt{2}$. At $T = 0$ K, we have for the filling factors

$$\langle n_{0,\chi}(k) \rangle = \Theta(k_{F,\chi} + \chi k), \quad (\text{B1})$$

$$\langle n_{n>0,s=-1,\chi}(k) \rangle = 1, \quad (\text{B2})$$

$$\langle n_{n>0,s=1,\chi}(k) \rangle = 0, \quad (\text{B3})$$

where $\Theta(x)$ the step function. We have defined $k_{F,\chi}$ as the Fermi wave vector measured with respect to the Dirac point in the node considered. Depending on the choice of b_0 and $e_{F,\chi}$, electrons or holes can be present in a node. After a lengthy but straightforward calculation, we obtain the following expressions for the interband contribution to the conductivity tensor and for $\omega > 0$ (the solution for $\omega < 0$ can be obtained by symmetry)

$$\text{Re}[\sigma_{xx}(\omega_r)] = \frac{e^2}{\hbar l} \frac{1}{8\pi\omega_r} \left[\Theta\left(\omega_r - \left(x_F + \sqrt{x_F^2 + 2}\right)\right) + \Theta\left(\omega_r - \left(-x_F + \sqrt{x_F^2 + 2}\right)\right) \right] \quad (\text{B4}) \\ + \frac{e^2}{\hbar l} \sum_{n>1} \frac{\omega_r^4 - 4}{16\pi\omega_r^3} \sum_{\pm} \frac{\left(1 + \frac{x_{\pm}}{e_n(x_{\pm})}\right) \sqrt{1 + \frac{x_{\pm}}{e_{n+1}(x_{\pm})}} \sqrt{1 + \frac{x_{\pm}}{e_{n-1}(x_{\pm})}}}{\sqrt{(\omega_r^2 + 2)^2 - 8\omega_r^2 n}} \Theta(\omega_r - \Delta_n(0)),$$

$$\text{Im} [\sigma_{xx} (\omega_r)] = \frac{e^2}{\hbar\ell} \frac{1}{8\pi^2\omega_r} \left[\log \left[\left| \frac{\omega_r^4 - 4\omega_r^2 x_F^2 - 4\omega_r^2 + 4}{4} \right| \right] + \omega_r^2 \sum_{n>1} 2 \int_{-\infty}^{+\infty} dx \frac{\Lambda_n(x)}{\Delta_n(x)} \frac{1}{\omega_r^2 - \Delta_n(x)^2} \right], \quad (\text{B5})$$

$$\text{Re} [\sigma_{xy} (\omega_r)] = -\frac{e^2}{\hbar\ell} \frac{1}{8\pi^2\omega_r} \log \left[\left| \frac{2 - \omega_r^2 + 2\omega_r x_F}{2 - \omega_r^2 - 2\omega_r x_F} \right| \right], \quad (\text{B6})$$

$$\text{Im} [\sigma_{xy} (\omega_r)] = \frac{e^2}{\hbar\ell} \frac{1}{8\pi\omega_r} \left[\Theta \left(\omega_r - \left(x_F + \sqrt{x_F^2 + 2} \right) \right) - \Theta \left(\omega_r - \left(-x_F + \sqrt{x_F^2 + 2} \right) \right) \right], \quad (\text{B7})$$

$$\text{Re} [\sigma_{zz} (\omega_r)] = \frac{e^2}{\hbar\ell} \frac{1}{2\pi} \sum_{n>0} \frac{2n}{\omega_r^2 \sqrt{\omega_r^2 - 8n}} \theta \left(\omega_r - 2\sqrt{2n} \right), \quad (\text{B8})$$

$$\text{Im} [\sigma_{zz} (\omega_r)] = \frac{e^2}{\hbar\ell} \frac{\omega_r}{\pi^2} \sum_{n>0} n \int_0^{+\infty} dx \frac{1}{(x^2 + 2n)^{3/2}} \frac{1}{\omega_r^2 - 4(x^2 + 2n)}, \quad (\text{B9})$$

These formulas are for one node and $x_F \equiv k_F \ell$. We have also defined the functions

$$e_n(x) = \sqrt{x^2 + 2n}, \quad (\text{B10})$$

$$\Delta_n(x) = e_n(x) + e_{n-1}(x), \quad (\text{B11})$$

$$x_{n,\pm} = \pm \sqrt{\left(\frac{\omega_r^2 + 2}{2\omega_r} \right)^2 - 2n}, \quad (\text{B12})$$

$$\Lambda_n(x) = \left(1 + \frac{x}{e_n(x)} \right) \sqrt{1 + \frac{x}{e_{n+1}(x)}} \quad (\text{B13})$$

$$\times \sqrt{1 + \frac{x}{e_{n-1}(x)}}. \quad (\text{B14})$$

Using the definitions of the eigenspinors given in the main text, it is easy to show that the only difference between the contribution of both nodes to the conductivity comes from the difference in the local Fermi wave vector $k_{F,\chi}$ which depends on the Fermi level e_F and b_0 through Eq. (13).

Defining a dimensionless conductivity tensor $\bar{\sigma}_{\chi,(\alpha\beta)}$ by

$$\sigma_{\chi,(\alpha\beta)}(\omega) = \frac{e^2}{\hbar\ell} \bar{\sigma}_{\chi,(\alpha\beta)}(\omega), \quad (\text{B15})$$

we have for the dielectric tensor of the two nodes

$$\varepsilon_{\alpha\beta} = \delta_{\alpha\beta} + \frac{2\pi^2 \kappa i}{\omega_r v_{F,r}} \sum_{\chi} \bar{\sigma}_{\chi,(\alpha\beta)}(\omega). \quad (\text{B16})$$

As in Appendix A, the contribution of the intra-Landau-level transitions in $n = 0$ to the conductivity

tensor must be calculated by including disorder. In our case, the intraband transitions are present only in the matrix element $\Gamma_{\chi;0;0}^{(z)}(k)$ so that we need to include disorder only in $\chi_{\chi}^{(z,z)}(\omega)$. We have for the intra-Landau-level current response function for one node

$$\chi_{\chi,(zz)}(\omega) = \frac{e^2}{2\pi\ell^2\hbar^2} \int \frac{dk}{2\pi} \left| \Gamma_{\chi;0;0}^{(z)}(k) \right|^2 \times \int_{-\infty}^{+\infty} d\omega' \int_{-\infty}^{+\infty} d\omega'' A_{\chi,0}(k, \omega') A_{\chi,0}(k, \omega'') \times \frac{F(\omega'') - F(\omega')}{\omega + i\delta + \omega'' - \omega'}. \quad (\text{B17})$$

We again choose a Lorentzian for the spectral weight which is given by

$$A_{\chi,0}(k, \omega) = \frac{\Gamma/\pi}{(\omega - (E_{\chi,0}(k) - e_{F,\chi})/\hbar)^2 + \Gamma^2} \quad (\text{B18})$$

and $e_{F,\chi}$ is the local Fermi level measured with respect to the Dirac point in node χ . At $T = 0$ K,

$$\chi_{\chi,(zz)}(\omega) = \frac{e^2}{\hbar^2} \frac{1}{2\pi\ell^2} \int \frac{dk}{2\pi} \left| \Gamma_{\chi;0;0}^{(z)}(k) \right|^2 \times \left[\int_{-\infty}^{e_{F,\chi}/\hbar} d\omega' a_{\chi}(k, \omega') g_{\chi}(k, \omega' + \omega) + \int_{-\infty}^{e_{F,\chi}/\hbar} d\omega' a_{\chi}(k, \omega') g_{\chi}(k, \omega' - \omega) - i\pi \int_{e_F/\hbar - \omega}^{e_F/\hbar} d\omega' a_{\chi}(k, \omega') a_{\chi}(k, \omega' + \omega) \right], \quad (\text{B19})$$

with the functions

$$a_{\chi}(k, \omega) = \frac{\Gamma/\pi}{(\omega - E_{\chi,0}(k)/\hbar)^2 + \Gamma^2} \quad (\text{B20})$$

and

$$g_{\chi}(k, \omega) = \frac{\omega - E_{\chi,0}(k)/\hbar}{(\omega - E_{\chi,0}(k)/\hbar)^2 + \Gamma^2}. \quad (\text{B21})$$

Evaluating these expressions analytically, we get for

the intra-Landau-level conductivity

$$\sigma_{\chi,(zz)}(\omega) = \frac{e^2 v_F \tau}{\hbar \ell 4\pi^2 \ell} \frac{1}{1 - i\omega\tau}. \quad (\text{B22})$$

This expression is independent of e_F and b_0 i.e., the same for both nodes.

-
- ¹ For a review of Weyl semimetals, see, for example : P. Hosur and X.-L. Qi, C. R. Physique **14**, 857-870 (2013); N. P. Armitage, E. J. Mele, A. Vishwanath, Rev. Mod. Physics **90**, 15001 (2018).
- ² H. B. Nielsen and M. Ninomiya, Phys. Lett. B **105**, 219 (1981).
- ³ K.Y. Yang, Y.M. Lu, Y. Ran, Phys. Rev. B **84**, 075129 (2011); G. Xu, H. Weng, Z. Wang, X. Dai, Z. Fang, Phys. Rev. Lett. **107**, 186806 (2011); P. Goswami, S. Tewari, Phys. Rev. B **88**, 245107 (2013); A.A. Burkov, L. Balents, Phys. Rev. Lett. **107**, 127205 (2011); A.A. Zyuzin, S.Wu, A.A. Burkov, Phys. Rev. B **85**, 165110 (2012).
- ⁴ J.H. Zhou, H. Jiang, Q. Niu, J.R. Shi, Chinese Phys. Lett. **30**, 027101 (2013); Y. Chen, S. Wu, A.A. Burkov, Phys. Rev. B **88**, 125105 (2013).
- ⁵ X. Wan, A.M. Turner, A. Vishwanath, S.Y. Savrasov, Phys. Rev. B **83**, 205101 (2011); P. Hosur, Phys. Rev. B **86**, 195102 (2012).
- ⁶ H. Z. Lu, S. B. Zhang and S. Q. Shen, Phys. Rev. B **92**, 045203 (2015); F. Wilczek, Phys. Rev. Lett. **58**, 1799 (1987).
- ⁷ D. T. Son and B. Z. Spivak, Phys. Rev. B **88**, 104412 (2013).
- ⁸ D. Cheskis, Symmetry, **12**, 1412 (2020).
- ⁹ X. Han, A. Markou, J. Stensberg, Y. Sun, C. Felser, and L. Wu, Phys. Rev. B **105**, 174406 (2022).
- ¹⁰ F. Wilczek, Phys. Rev. Lett. **58**, 1799 (1987).
- ¹¹ L. Wu, M. Salehi, N. Koirala, J. Moon, S. Oh, and N. P. Armitage, Science **354**, 1124 (2016).
- ¹² A. A. Zyuzin and A. A. Burkov, Phys. Rev. B **86**, 115133 (2012); Y. Chen, Si Wu, and A. A. Burkov, Phys. Rev. B **88**, 125105 (2013).
- ¹³ M. Kargarian, M. Randeria and N. Trivedi, Sci. Rep. **5**, 12683 (2015).
- ¹⁴ K. Sonowal, A. Singh, and A. Agarwal, Phys. Rev. **100**, 085436 (2019).
- ¹⁵ J.-M. Parent, R. Côté, and I. Garate, Phys. Rev. B **102**, 245126 (2020).
- ¹⁶ S. Bertrand, J.-M. Parent, R. Côté, and I. Garate, Phys. Rev. B **100**, 075107 (2019).
- ¹⁷ M. Balkanski and R. F. Wallis, *Many-Body Aspects of Solid State Spectroscopy* (North-Holland, Amsterdam, 1986).
- ¹⁸ P. E. C. Ashby and J. P. Carbotte, Phys. Rev. B **89**, 245121 (2014).
- ¹⁹ C. J. Tabert, J. P. Carbotte, and E. J. Nicol, Phys. Rev. B **93**, 085426 (2016).
- ²⁰ S. P. Mukherjee and J. P. Carbotte, Phys. Rev. B **97**, 035144 (2018).
- ²¹ A. Singh and J. P. Carbotte, Phys. Rev. B **103**, 075114 (2021).
- ²² S. Tchoumakov, M. Civelli and M. O. Goerbig, Phys. Rev. Lett. **117**, 086402 (2016).
- ²³ J. Ma and D. A. Pesin, Phys. Rev. B **92**, 235205 (2015).
- ²⁴ S. Zhong, J. E. Moore, and I. Souza, Phys. Rev. Lett. **116**, 077201 (2016).
- ²⁵ O. V. Kotov and Y. E. Lozovik, Phys. Rev. B **93**, 235417 (2016).
- ²⁶ D. Sa, Eur. Phys. J. B **94**, 31 (2021).
- ²⁷ K. Deng, J. S. Van Dyke, D. Minic, J. J. Heremans, and E. Barnes, Phys. Rev. B **104**, 075202 (2021).
- ²⁸ M. Born and W. Wolf, *Principles of optics*, (Cambridge University Press, 1980).
- ²⁹ A. L. Levy, A. B. Sushkov, F. Liu, B. Shen, N. Ni, H. D. Drew and G. S. Jenkins, Phys. Rev. B **101**, 125102 (2020).
- ³⁰ F. Arnold, M. Naumann, S.-C. Wu, Y. Sun, M. Schmidt, H. Borrmann, C. Felser, B. Yan, and E. Hassinger, Phys. Rev. Lett. **117**, 146401 (2016).
- ³¹ P. Li, Y. Wen, X. He, Q. Zhang, C. Xia, Z.-M. Yu, S. A. Yang, Z. Zhu, H. N. Alshareef, and X.-X. Zhang, Nat. Commun. **8**, 2150 (2017).
- ³² X. Huang, H. Geng, and L. Sheng, Phys. Rev. B **103**, 115208 (2021).
- ³³ S. Das Sarma, E. H. Hwang, Phys. Rev. Lett. **102**, 206412 (2009); M. Lv, S. C. Zhang, Int. J. Mod. Phys. B **27**, 1350177 (2013) ; J. Hofmann and S. Das Sarma, Phys. Rev. B **91**, 241108(R) (2015).
- ³⁴ J. Zhou, Hao-Ran Chang, D. Xiao, Phys. Rev. B **91**, 035114 (2015).
- ³⁵ F. M. D. Pellegrino, M. I. Katsnelson, and M. Polini, Phys. Rev. B **92**, 201407(R) (2015).
- ³⁶ Z. Qiu, G. Cao, and X.-G. Huang, Phys. Rev. D **95**, 036002 (2017).
- ³⁷ Y. Okamura, S. Minami, Y. Kato, Y. Fujishiro, Y. Kaneko, J. Ikeda, J. Muramoto, R. Kaneko, K. Ueda, V. Kocsis, N. Kanazawa, Y. Taguchi, T. Koretsune, K. Fujiwara, A. Tsukazaki, R. Arita, Y. Tokura and Y. Takahashi, Nat. Commun. **11**, 4619 (2020).
- ³⁸ Q. Wang, Y. Xu, R. Lou, Z. Liu, M. Li, Y. Huang, D. Shen, H. Weng, S. Wang, and H. Lei, Nat Commun **9**, 3681 (2018).
- ³⁹ L.-L. Wang, N. H. Jo, B. Kuthanazhi, Y. Wu, R. J. McQueeney, A. Kaminski, and P. C. Canfield, Phys. Rev. B **99**, 245147 (2019).
- ⁴⁰ Soh, J.R., deJuan, F., Vergniory, M.G., Schroter, N.B.M., Rahn, M.C., Yan, D.Y., Jiang, J., Bristow, M., Reiss, P., Blandy, J.N., Guo, Y.F., Shi, Y.G., McCollam, A., Simon, S.H., Chen, Y., Coldea, A.I., Boothroyd, A.T., Phys. Rev. B **100**, 201102(R), (2019).
- ⁴¹ S. Nie, T. Hashimoto, and F. B. Prinz, Phys. Rev. Lett. **128**, 176401 (2022).
- ⁴² P. E. C. Ashby and J. P. Carbotte, Phys. Rev. **87**, 245131 (2013).